A septo-hypothalamic-medullary circuit directs stress-induced analgesia

Devanshi Piyush Shah[1], Pallavi Raj Sharma[2], Rachit Agarwal[3], and Arnab Barik[4]

Abstract

Stress is a potent modulator of pain. Specifically, acute stress due to physical restraint induces stress-induced analgesia (SIA). However, where and how acute stress and pain pathways interface in the brain are poorly understood. Here, we describe how the dorsal lateral septum (dLS), a forebrain limbic nucleus, facilitates SIA through its downstream targets in the lateral hypothalamic area (LHA) of mice. Taking advantage of transsynaptic viral-genetic, optogenetic, and chemogenetic techniques, we show that the dLS→LHA circuitry is sufficient to drive analgesia and is required for SIA. Further, our results reveal that the dLS→LHA pathway is opioid-dependent and modulates pain through the pro-nociceptive neurons in the rostral ventromedial medulla (RVM). Remarkably, we found that the inhibitory dLS neurons are recruited specifically when the mice struggle to escape under restraint and, in turn, inhibit excitatory LHA neurons. As a result, the RVM neurons downstream of LHA are disengaged, thus suppressing nociception. Together, we delineate a poly-synaptic pathway that can transform escape behavior in mice under restraint to acute stress into analgesia.

[1, 4]Centre for Neuroscience, Indian Institute of Science, Bengaluru, Karnataka, India - 560012
[2, 3]Centre for BioSystems Science and Engineering, Indian Institute of Science, Bengaluru, Karnataka, India - 560012

[4]Corresponding author: arnabbarik@iisc.ac.in

Introduction

Descending modulation of pain is the mechanism through which the brain imparts control over somatosensory information processing in the spinal cord. Forebrain and midbrain regions encoding internal states such as stress and hunger can harness the brainstem circuits that project to the spinal cord neurons to alleviate pain (Tracey and Mantyh, 2007). Such analgesic mechanisms are critical for survival since they prepare animals and humans to cope with the stressors or enable them to meet their physiological needs on time. Moreover, harnessing the underlying modulatory mechanisms may lead us to novel therapeutic approaches for chronic pain. Stress Induced Analgesia (SIA) is one such incidence where an acute stressor, such as physical restraint, can result in analgesia. However, the neural mechanisms that facilitate SIA remain poorly understood.

Experiments involving human subjects in the 1950s and 1960s have shown that direct electrical stimulation of the dorsal lateral septum (dLS) has anti-nociceptive (Gol, 1967; Olds and Milner, 1954) effects. In rats, dLS activation suppressed behavioral responses to foot-shocks (Vincent Breglio et al., 1970) or sustained noxious stimuli such as intraplantar formalin injections (Abbott and Melzack, 1978). Further, septum inactivation or lesion renders rats hypersensitive to sensory stimuli, and as a result, they display exaggerated stimulus-driven defensive responses (Albert and Wong, 1978; Köhler, 1976). dLS neurons receive nociceptive inputs from the thalamus and somatosensory cortices, as well as anxiogenic information from the hypothalamus. Neurotensin expressing dLS neurons with projections to the lateral hypothalamic area (LHA) mediate acute stress mediated suppression of food consumption (Azevedo et al., 2020). Despite these convincing leads indicating the involvement of dLS neurons in the processing of noxious somatosensory stimuli, mechanistic investigation of the role of dLS in nociception remains scarce. Classical studies involving lesions to lateral parts of the septal nucleus resulted in a phenomenon known as septal rage, which leads to heightened defensive responses against non-threatening stimuli, indicative of increased levels of stress and anxiety (Brady and Nauta, 1953); (Brady and Nauta, 1955). Interestingly, dLS is essential to sensing acute stress and instrumental in stress-induced fear and anxiety (Anthony et al., 2014; Rizzi-Wise and Wang, 2021; Sheehan et al., 2004); (Terrill et al., 2018). This involvement of dLS in acute stress-induced anxiety is reflected in behavioral phenotypes and the elevated blood corticosterone levels (Singewald et al., 2011). Taken together, dLS neurons were shown independently to mediate the effects of both nocifensive behaviors and acute stress. However, the role of dLS neurons in pain modulation in the event of an ongoing stressful stimulus remains unexplored. Hence, we hypothesized that dLS might play a facilitatory role in SIA.

The dLS neurons communicate primarily through their inhibitory neurotransmitters and have prominent projections to brain areas involved in nociception and pain processing (Rizzi-Wise and Wang, 2021). Of note are the projections to the lateral habenula (LHb) and the LHA (Dafny et al., 1996; Shelton et al., 2012). The midbrain LHb can modulate the affective aspects of pain via its projections to the brainstem periaqueductal gray (PAG) and dorsal raphe (Shelton et al., 2012). LHA neurons have strong connections to the pain-modulatory nuclei in the brainstem, such as the rostral ventromedial medulla (RVM) and the lateral parabrachial nuclei (LPBN). In addition, recent studies have reported that LHA neurons can sense noxious stimuli and suppress pain (Siemian et al., 2021); (Carr and Uysal,

1985), and specifically, the projections to the RVM were shown to have anti-nociceptive effects (Behbehani et al., 1988; Dafny et al., 1996; Franco and Prado, 1996; Fuchs and Melzack, 1995; Holden and Pizzi, 2008). The LPBN neurons are one of the primary targets of the ascending nociceptive projection neurons from the dorsal horn of the spinal cord (Todd, 2010). They are instrumental in determining nociceptive thresholds (Chiang et al., 2020) and mediating nocifensive behaviors (Barik et al., 2018; Arthurs et al., 2023; Han et al., 2015). Thus, we reasoned that the dLS→LHA circuitry, through downstream circuits, may mediate SIA.

Here, we have explored the mechanisms through which acute restraint stress (RS)-responsive dLS neurons recruit downstream circuits to provide pain relief. Taking advantage of the anterograde trans-synaptic and retrogradely transporting viral genetic tools for anatomic circuit mapping, we have traced a pathway that originates in the dLS, and routes through LHA while finally terminating onto the spinally-projecting RVM neurons. Optogenetic and chemogenetic manipulations of the activity of each node of this pathway informed us on how they play interdependent roles in transforming restrain-induced stress into the suppression of acute thermal pain. Fiber photometry recordings revealed how the inhibitory dLS neurons may suppress the excitatory LHA neurons upon stress, which can disengage pro-nociceptive RVM cells, resulting in analgesia. Taken together, our data propose a mechanism that can explain how RS can suppress pain and lead to understanding how the circuitries dedicated to detecting stress can interface with the ones built for modulating pain.

Results

dLS neurons drive acute stress and SIA

The dLS neurons have been known to be engaged by stressful stimuli such as physical restraint (Azevedo et al., 2020). To confirm this, we compared the expression of c-Fos, a molecular proxy for neural activation, in the dLS of control mice with the mice subjected to the RS assay (see methods). Mice that underwent RS showed increased cFos expression in the dLS as compared to the control unstressed mice (Figures 1A, 1B, 1C). This suggests that dLS neurons may be involved in mediating acute stress, in agreement with previous studies (Azevedo et al., 2020; Kubo et al., 2002). Notably, internal states, such as stress, can determine nociceptive thresholds (Amit and Galina, 1986; Butler and Finn, 2009). Despite extensive investigation into the dLS's role in stress, not much is known about the involvement of these neurons in pain modulation. Thus, we tested if artificial stimulation of the dLS neurons in CD1 strain of mice can affect the animal's latency to response on the tail-flick test and nocifensive behaviors such as licks on the hot-plate test. Tail-flick and hot-plate tests can reveal the involvement of spinal and supraspinal circuitries in behavioral responses to noxious thermal stimuli, respectively. Since most of the dLS neurons are inhibitory (Figure 1D), we expressed the Gq-coupled excitatory Designer Receptors Exclusively Activated by Designer Drugs (DREADD) hM3Dq (Alexander et al., 2009) under the inhibitory neuron-specific Gad67 promoter (dLSGad67-hM3Dq-mCherry) (Figures 1E, 1F). Upon intraperitoneal (i.p.) administration of the ligands CNO or DCZ, hM3Dq enables neuronal firing. When dLS neurons were activated by administration of i.p. DCZ (Alexander et al., 2009; Nagai et al., 2020), the mice exhibited stress and stress-induced anxiety-like behaviors as confirmed by blood corticosterone levels (Figure S1A), the light-dark box test (Figure S1B, S1C), and the open field test (Figures S1D, S1E). Nocifensive behaviors like licks on the hotplate were suppressed post-DCZ administration in dLSGad67-hM3Dq-mCherry mice, with no changes in the jumping behavior (Figures S1G, S1H). The tail flick latency in these mice was significantly increased, number of licks on the hotplate reduced and the latency to lick initiation increased (Figures 1G, 1H). Mice with activated dLS neurons showed higher thresholds for mechanical pain (Figure S1F). Similar changes in mice behavior were observed when these tests were combined with optogenetic activation of the dLS neurons (dLSGad67-ChR2-GFP) (Figures S1I-L). Further, it was seen that the analgesic effects of dLS neurons lasted for up to 30 minutes post optogenetic activation (Figure S2A), and this timeline was like the analgesic effects induced by RS (Figure S2B). Concluding, that the RS induced thermal analgesia and pain-modulation attained by artificial activation of dLS neurons are comparable. This phenomenon, known as SIA, has previously not been associated with the septal neurons. Further, to investigate whether these dLS neurons are necessary for bringing about SIA, we blocked the spike-evoked neurotransmitter release of dLS neurons by expressing the tetanus toxin light chain protein fused with GFP (TetTox-GFP) (dLSGad67-TetTox-GFP) (Campos et al., 2018; Xu et al., 2012) (Figures 1I, 1J). The efficacy of the tetanus toxin virus was confirmed by testing its effect on mouse behavior in pairing with the excitatory DREADD hM3Dq (Figure S2C, S2D). Post-silencing of the dLS neurons, we observed that the stress caused by RS was unable to cause analgesia that was previously seen on both the tail flick assay and the hotplate test (Figures 1K, 1L). Again, no

difference was seen in the jumping behavior of the mice (Figures S2E-G). Concluding, that the dLS neurons are both sufficient and necessary for SIA.

Next, we probed if the dLS neurons are engaged by RS and/ or noxious stimuli. To that end, we expressed the genetically encoded calcium sensor GCaMP6s (Chen et al., 2013) in the dLS neurons (dLSGad67-GCaMP6s) (Figures 2A, 2B), and performed fiber photometry recordings (Figure 2C). Fiber photometry enables activity monitoring from the genetically and anatomically defined neuronal population in behaving mice and can provide critical insights into how neural activity corresponds to animal behavior in response to a particular stimulus (Lerner et al., 2015). As expected, we observed spontaneous transients in the dLS neurons of mice expressing GCaMP6s but not in the neurons with GFP (Figure 2D). Notably, in mice under RS, dLSGad67-GCaMP6s neurons were active only when the animals in the RS assay apparatus (see methods) struggled and not when they were freely moving in their home cages (Figures 2E, 2F, 2G, S3, S3B). This suggests that the increased neural activity during the struggle bouts in mice under RS is not simply due to the increased physical activity but due to the need and inability to escape the restraint (Figures S3A, S3B). Similarly, we restrained the mice acutely by hand, and dLSGad67-GCaMP6s neurons were active during the initial immobilization phase while the mice struggled, after which the activity was reduced when they were unable to move due to the restraint (Figures S3C, S3D). The neurons were active again when the mice were released from the hand restraint and were free to run away (Figures S3C, S3D). Thus, in agreement with the previous result, the dLSGad67-GCaMP6s neurons were active when the mice actively struggled to escape any physical restraint. Another acute stress assay that engaged the dLSGad67-GCaMP6s neurons was the tail hanging assay, wherein mice were suspended in air by holding their tails for 10 seconds (Figures S3C, S3D). Since artificial stimulation or blocking dLSGad67 neuronal activity had suppressive effects on pain thresholds, we next tested if the dLSGad67-GCaMP6s neurons respond to noxious thermal stimuli (52 degrees for one minute on the hot plate). The dLSGad67-GCaMP6s neurons were found to be inactive during the hot-plate test at innocuous (Figures 2H, 2I), as well as at a noxious temperature when the mice exhibited nocifensive behaviors such as licks and shakes (Figures 2J, 2K). Thus, from our fiber photometry data, we concluded that the dLSGad67-GCaMP6s neurons are preferentially tuned to stress caused by physical restraint and not to noxious thermal stimuli.

dLS neurons facilitate SIA through downstream LHA neurons

In the following experiments, we sought to determine the postsynaptic targets through which dLS neurons signal and facilitate RS-induced analgesia. To address this, we mapped the axonal targets of dLSGad67 neurons by labeling these neurons with cell-filing GFP (dLSGad67-GFP) (Figures 3A, 3B). In agreement with previous reports, we observed dLSGad67-GFP axon terminals in the LHA, the habenula (Hb), and the hippocampus (Figures 3C) (Amit and Galina, 1986; Kubo et al., 2002). To confirm that the axonal terminals of the dLS neurons at the targets form synapses with the neurons in the LHA, Hb, and hippocampal formation we labeled the axon terminals of dLSGad67 neurons with synaptophysin fused with the red fluorescent protein ruby (dLSGad67-SynRuby) (Figure S4A) and found SynRuby puncta in all aforementioned dLSGad67 axonal targets (Figure S4B), suggesting that dLS neurons synapse onto its downstream LHA (Figure S4C), Hb, and

hippocampal neurons. We hypothesized that the dLS neurons may exert their analgesic effects through downstream LHA and/ or Hb connections for following reasons: firstly, both LHA and Hb neurons have been implicated in determining nociceptive thresholds (Singewald et al., 2011); (Butler and Finn, 2009); second, LHA and Hb have direct connections to pain modulatory regions in the brain stem such as the PAG, the RVM, and the dorsal raphe nucleus (DRN) (Singewald et al., 2011); (Ma et al., 1992); third, LHA and Hb contain pro-nociceptive neurons, inhibition of which can cause analgesia (Benabid and Jeaugey, 1989; Mahieux and Benabid, 1987); and fourth, the role of hippocampal neurons in pain modulation is less clear.

To test if dLS modulates nociceptive thresholds through its projections to the LHA, we selectively stimulated the axon terminals of the dLSGad67 neurons in the LHA by expressing ChR2 in the dLS (dLSGad67-ChR2) and shining blue light on the terminals at LHA through fiber optic cannulae (Figure 3D). Selective activation of the dLSGad67-ChR2terminals in the LHA resulted in increased latency on the tail-flick assay (Figure 3E) and a reduced number of licks with an increased threshold on the hot-plate assay (Figure 3F), suggestive of analgesia. These observations were like the results from the experiments where the cell bodies of dLSGad67-ChR2 neurons were stimulated (Figures S1I-L). Taken together, these results suggest that stimulating dLSGad67 cell bodies or their axon terminals in the LHA is sufficient to cause analgesia. In complementary experiments, we chemogenetically activated dLSGad67 terminals in the LHA. To that end, we devised a novel microparticle (MP)-based delivery system (Jain, 2000; Sharma et al., 2022) for CNO (for the MP-based delivery system, hM3Dq agonist CNO was used due to greater hydrophobicity, which is essential for MP packaging, compared to DCZ), which can be injected specifically in the LHA where dLS neurons terminate (Figures S5 A-C). Compared to the widely-used method for in-vivo drug delivery at deep brain nuclei through cannulae (Campbell and Marchant, 2018; Stachniak et al., 2014), our poly-DL-lactic-co-glycolic (PLGA) microparticle (MP-CNO) based system (see methods) can serve as a stable, cost-effective, non-invasive, site-specific, and sustained method for CNO delivery. To demonstrate the efficacy of the MP-CNO, we stereotaxically injected MP-CNO in the dLS of dLSGad67-hM3Dq and recorded cFos expression in the dLS to confirm that the beads were able to activate the neurons. We observed peak cFos expression at Day 4 (Figure S5D), which is in agreement with our observations of analgesic behavior in the mice. In the dLSGad67-hM3Dq mice, MP-CNO was analgesic, and the effects were pronounced between 48-96 hours of delivery (Figures S5E, F). Remarkably, the MP-CNO-induced analgesia was comparable to that of i.p. CNO administration (Figures S5H, I). The control mice (dLSGad67-tdTomato) did not demonstrate any difference in behavior over days (Figure S5G-I). Finally, we delivered MP-CNO in the LHA of dLSGad67-hM3Dq mice for terminal activation and observed increased tail-flick thresholds, fewer licks, and higher lick thresholds (Figures S5J-L). Thus, our acute optogenetic and chronic chemogenetic axon terminal activation experiments demonstrate that dLS neurons could bring about analgesia through their projections to the LHA.

Next, we chemogenetically stimulated the dLS neurons whose axon terminals arborize and synapse onto the LHA neurons ($dLS_{pre\text{-}LHA}$). To that end, we injected retrogradely transporting AAV (AAVRetro-Cre) in the LHA and DIO-hM3Dq-mCherry in the dLS. This intersectional genetic strategy facilitated excitatory DREADD expression exclusively in

$dLS_{pre\text{-}LHA}$ neurons ($dLS_{pre\text{-}LHA}$hM3Dq-mCherry) (Figure 3G). i.p administration of DCZ in the dLS $_{pre\text{-}LHA}$hM3Dq-mCherry mice had similar analgesic effects as seen with dLSGad67 activation (Figures 3H, 3I), indicating that activation of a specific subset of dLS neurons ($dLS_{pre\text{-}LHA}$) is sufficient for altering thermal nociception in mice. In the following experiments, we asked what the effect of chemogenetic activation of the LHA neurons downstream of dLS ($LHA_{post\text{-}dLS}$) on thermal nociceptive thresholds would be. To address this, we chemogenetically activated $LHA_{post\text{-}dLS}$ neurons by injecting AAVTrans-Cre in the dLS and AAV-DIO-hM3Dq-mCherry in the LHA (Figure 3J). I.p. administration of DCZ in mice expressing hM3Dq in $LHA_{post\text{-}dLS}$ neurons reduced the latency to react on the tail-flick assay, increased the number of licks, and decreased the latency to lick on the hot-plate test (Figures 3K, 3L). Intriguingly, our data suggest that when activated, dLSGad67 neurons inhibit LHA neurons to cause analgesia, and so when $LHA_{post\text{-}dLS}$ neurons are artificially activated, it has the opposite effect on nocifensive behaviors and leads to hyperalgesia. In addition, given that dLS neurons project to the Hb (Figure 3C) and Hb neurons have been shown to have anti-nociceptive effects (Cohen and Melzack, 1985), we tested if activating Hb neurons post-synaptic to dLS ($Hb_{post\text{-}dLS}$) can alter thermal pain thresholds (Figure 3M). DCZ administration had no effect on thermal pain thresholds in $Hb_{post\text{-}dLS}$hM3Dq mice (Figures 3N, 3O). Further, we tested the effects of silencing the $LHA_{post\text{-}dLS}$ neurons on RS-induced SIA (Figure 3P). TetTox mediated $LHA_{post\text{-}dLS}$ silencing abolished SIA (Figures 3Q, 3R). In summary, the $LHA_{post\text{-}dLS}$ neurons are functionally downstream of dLSGad67 neurons, and simultaneous transient activation has identical effects on nociceptive thresholds.

dLS neurons synapse onto the Vesicular glutamate transporter 2 (Vglut2)-expressing LHA neurons

We then tested if the LHA neurons receiving inputs from dLS are excitatory or inhibitory, given that LHA is composed of both VGlut2 and Vesicular Gamma-aminobutyric acid (GABA) Transporter (VGat) expressing neurons (Figures S6A, S6B), with a relatively smaller population of VGlut2-positive neurons (Figures S6A, S6B), which have recently been implicated in pain modulation (Singewald et al., 2011). To test if VGlut2+ LHA neurons receive direct inputs from dLSGad67neurons, we took three complementary approaches. First, we injected AAV1-FlpO with anterograde transsynaptic transmission properties (AAV1-hSyn-FlpO or Transyn-FlpO) (Alexander et al., 2009; Campos et al., 2018; Nagai et al., 2020) in the dLS of VGlut2-Cre transgenic mice (Figure 4A). Simultaneously, we injected DIO-GFP and fDIO-tdTomato in the LHA of the same mice (Figure 4A). We found that 34.2 ± 9.6 % (n = 8 sections, 3 mice) tdTomato expressing cells ($LHA_{post\text{-}dLS}$) were GFP +ve, indicative of their excitatory status (Figure 4B). Second, we delivered anterograde transsynaptic Cre (AAV1-hSyn-Cre or Transyn-Cre) in the dLS of Rosa26-LSL-tdTomato transgenic mice to label the $LHA_{post\text{-}dLS}$ neurons with tdTomato and performed multiplex fluorescent in-situ hybridization for VGlut2 and tdTomato mRNA in the LHA (Figure 4C). We found that 28.5 ± 11.2 % (n = 12 sections, 2 mice) tdTomato neurons colocalized with VGlut2 (Figure 4D). Third, we labeled the synaptic terminals of dLSGad67 neurons and post-synaptic densities of LHAVGlut2 neurons by expressing synaptophysin-fused GFP (SynGFP) in the dLSGad67 neurons and Cre-dependent inhibitory postsynaptic protein, Gephyrin fused with red fluorescent protein tagRFP (DIO-GephryrintagRFP) (Xu et al., 2012); (Chen et al.,

2013; Xu et al., 2012); (Lerner et al., 2015) in the LHA of VGlut2-Cre mice, respectively (Figure 4E). Here, we noticed close apposition of green synaptophysin and red gephyrin puncta in the LHA (Figure 4F), suggesting that dLSGad67 neurons make synaptic connections onto VGlut2 neurons in the LHA ($LHA_{post\text{-}dLS}$VGlut2). Overall, these results suggest that inhibitory dLS axons synaptically target the excitatory populations of LHA neurons. Since parvalbumin (PV) labels a subset of excitatory neurons in the LHA and PV-expressing neurons in the LHA have been shown to be antinociceptive (Singewald et al., 2011), we tested if $LHA_{post\text{-}dLS}$ neurons colocalize with PV-expressing cells and found little to no overlap between the two populations (Figure S6C). Together, our anatomical data indicate that the dLSGad67 neurons are synaptically connected with the VGlut2+ve neurons in the LHA.

$LHA_{post\text{-}dLS}$ neurons are inhibited upon acute restraint

Next, we reasoned that if $LHA_{post\text{-}dLS}$ neurons are inhibited by dLSGad67 neurons, then these neurons must be disengaged when mice undergo acute stress. To test this, we labeled $LHA_{post\text{-}dLS}$ neurons with GCaMP6s ($LHA_{post\text{-}dLS}$GCaMP6s) (Figures 5A, B) and recorded calcium transients from these neurons as mice underwent RS (Figure 5C) as well as when they were exposed to noxious thermal stimulus. Surprisingly, fiber photometry recordings showed that $LHA_{post\text{-}dLS}$GCaMP6s neurons respond to acute stress caused by physical restraint and tail hanging (Figures S7A-D). In addition, like dLSGad67 neurons (Figures 2H-K), $LHA_{post\text{-}dLS}$GCaMP6s neurons were not engaged by noxious thermal stimuli (Figures S7E-H). Notably, $LHA_{post\text{-}dLS}$GCaMP6s neurons differed in their activity from the dLSGad67-GCaMP6s neurons in one aspect — while mice struggled in the RS assay, dLSGad67-GCaMP6s neurons were active for the entire duration of the struggle bouts (up to 10 seconds) (Figure 5D), $LHA_{post\text{-}dLS}$GCaMP6s neurons were active only during the initial phase of the struggle (1-3 seconds) (Figure 5D). This indicates that activity of pre-synaptic dLS and post-synaptic $LHA_{post\text{-}dLS}$ neurons increases in a coordinated manner at the onset of struggle in mice undergoing RS-assay. However, after the initial activity, $LHA_{post\text{-}dLS}$ neurons can potentially be suppressed by inhibitory dLS inputs causing a reduction in the firing of these post-synaptic neurons. Taken together, these data suggest that acute stress inhibits a sub-population of excitatory neurons in the LHA that are postsynaptic to inhibitory dLS neurons.

$LHA_{post\text{-}dLS}$ neurons facilitate SIA through projections to RVM

Next, in order to investigate how $LHA_{post\text{-}dLS}$ neurons facilitate RS-induced analgesia, we mapped the projections of these neurons. Expression of GFP in the $LHA_{post\text{-}dLS}$ neurons, labeled axon-terminals in the LPBN, and the RVM (Figure 6 A-C). In previous studies, activation or silencing of LPBN neurons did not alter the reflexive withdrawal thresholds or coping responses, such as licks in response to noxious thermal stimuli (Barik et al., 2018; Chiang et al., 2020; Han et al., 2015). However, RVM neurons are known to modulate pain bi-directionally (Fields, 2004; François et al., 2017). Importantly, SIA is opioid-dependent (Finn, 2017; Lewis et al., 1981; Vaccarino et al., 1992) (Figure S8A), and RVM is a major substrate for endogenous opioids (Fields, 2004). We confirmed the opioid-dependent nature of SIA induced by septal activation, by simultaneous administration of mu-opioid receptor

antagonist naltrexone and DCZ in dLSGad67-hM3Dq mice, which lead to the blocking of dLS activation-induced analgesia (Figures S8B, S8C). Thus, we reasoned that the projections of the $LHA_{post\text{-}dLS}$ neurons synapse onto RVM neurons and facilitate RS-induced analgesia. To that end, first, we sought to establish the anatomical location and projections of the RVM neurons ($RVM_{post\text{-}LHA}$) — that are postsynaptic to the $LHA_{post\text{-}dLS}$ neurons. We labeled the $RVM_{post\text{-}LHA}$ neurons with GFP (Figure 6D) and SynRuby (Figure S8D) separately, using the anterograde intersectional viral genetic strategy used before (AAVTrans-Cre in LHA; DIO-GFP or DIO-SynRuby in RVM). We observed that the cell bodies of the $RVM_{post\text{-}LHA}$ neurons were distributed in the midline area (Figures 6E, S8E) of the medulla. We noticed abundant axon terminals of $RVM_{post\text{-}LHA}$ neurons in the LHA (Figure S8F), and projections in the deeper layers (VI/ VII) of the lumbar spinal cord (Figures 6F, S8G). This implies that the $RVM_{post\text{-}LHA}$ neurons may modulate nociceptive thresholds through their local synaptic connections within the RVM, recurrent connections with the PAG, or direct interactions with spinal cord neurons. Second, using the monosynaptic retrograde rabies tracing technique (Callaway and Luo, 2015; Wickersham et al., 2007), we determined if the $RVM_{post\text{-}LHA}$ neurons are the direct postsynaptic partners of the $LHA_{post\text{-}dLS}$ neurons. We expressed G and TVA-GFP proteins in $LHA_{post\text{-}dLS}$ neurons (AAVTransyn-Cre in dLS; DIO-G; DIO-TVA-GFP in LHA) and injected delG-Rabies-mCherry in the RVM (Figure 6G). As expected, we observed the starter cells that co-expressed TVA-GFP ($LHA_{post\text{-}dLS}$) and delG-Rabies-mCherry (retrogradely transported from the RVM; $LHA_{pre\text{-}RVM}$) in the LHA (Figure 6H). Remarkably, retrogradely transported Rabies-mCherry was found in the dLS neurons (Figure 6H). Indicating that the dLS neurons are directly upstream of the RVM projecting LHA neurons. Third, in a complementary approach, we took advantage of the GRASP synaptic labeling strategy (Kim et al., 2011), where presynaptic neurons expressed one-half of the GFP protein, and the postsynaptic neurons expressed the other half. At the functional synapses between the two GFP-subunit expressing neurons, GFP is reconstituted and can be visualized through a fluorescent microscope. In our experiments, we injected Pre-GRASP in the dLS, fDIO-Post-GRASP in the LHA, and AAVRetro-FlpO in the RVM (Figure 6I) of the same mice. Simultaneous injection of the three AAVs successfully labeled the synapses between the dLS and $LHA_{pre\text{-}RVM}$ neurons with GFP in the LHA (Figure 6J). Thus, demonstrating that the dLS neurons make synaptic connections with $LHA_{pre\text{-}RVM}$ neurons.
We then sought to understand how the $RVM_{post\text{-}LHA}$ neurons encode RS and noxious thermal stimuli, and thus, we performed fiber photometry recordings from the GCaMP6s expressing $RVM_{post\text{-}LHA}$ neurons ($RVM_{post\text{-}LHA\text{-}GCaMP6s}$) (Figures 7A, B). Calcium transients in the $RVM_{post\text{-}LHA}$ neurons increased spontaneously when the mice were subjected to RS (Figure 7C). However, when the mice struggled under restraint, $RVM_{post\text{-}LHA}$ neuronal activity was suppressed (Figures 7C, D). The activity of the $RVM_{post\text{-}LHA\text{-}GCaMP6s}$ neurons increased when the mice shook or licked their paws on the hot-plate test (Figure 7E). Notably, the rise in activity of the $RVM_{post\text{-}LHA}$ neurons preceded the licks and shakes, indicating a facilitatory role of these neurons in nocifensive behaviors. To further confirm this facilitatory role, performed two additional assays. First, we recorded calcium transients from the $RVM_{post\text{-}LHA\text{-}GCaMP6s}$ neurons while the mice were on the hot plate set to a gradient of 32-52 degrees over a period of 5 minutes. We observed that the neurons started firing only once the hot plate reached noxious temperatures, with no specific activity seen at innocuous temperatures

(Figure 7F). Second, we subjected the mice to the tail flick assay and observed a peak in neural firing preceding the tail flick instance caused by the thermal pain caused by the concentrated beam of light (Figure 7G). From these series of experiments, we were able to further confirm the facilitatory role of the $RVM_{post\text{-}LHA}$ neurons in nocifensive behaviors. The facilitatory pro-nociceptive population of RVM neurons is otherwise known as ON-cells (Fields et al., 1995, 1991) Thus, we hypothesized that these $RVM_{post\text{-}LHA}$ neurons are pro-nociceptive and likely ON cells. They are activated by acute stress and suppressed when the mice struggle to escape stress-causing restraint. When we calculated the area under the curve (AUC) of the Z-score of the recordings from the dLS, $LHA_{post\text{-}dLS}$, and $RVM_{post\text{-}LHA}$ neurons while the mice struggled in the RS assay, the data indicated that the dLS activity increased while at the same time $LHA_{post\text{-}dLS}$, and $RVM_{post\text{-}LHA}$ activity decreased (Figure S9E). Together, our data indicate that the LS inhibitory neurons engaged by acute restraint, suppresses LH activity which in turn reduces the excitability of the pronociceptive RVM neurons and result in analgesia.

To further establish that the $RVM_{post\text{-}LHA}$ neurons are ON cells, we chemogenetically activated the $RVM_{post\text{-}LHA}$neurons (Figures 8A, B). Mice expressing hM3Dq in the $RVM_{post\text{-}LHA}$ responded with increased licks on the hot-plate test and a lower latency when i.p. DCZ was administered (Figures 8C, D). Contrary to $RVM_{post\text{-}LHA}$ activation, when we chemogenetically and silenced the $RVM_{post\text{-}LHA}$ neurons (Figures 8E-H), the number of licks on the hot-plate test was reduced, and the latency to lick and the tail-flick latency were increased. These findings agree with our hypothesis that the activated dLS neurons inhibit $LHA_{post\text{-}dLS}$ neurons, which in turn deactivates $RVM_{post\text{-}LHA}$ cells. Moreover, the observation that silencing bi-lateral LPBN neurons postsynaptic to LHA (Figures 8I, 8J) did not affect mouse responses on hot-plate and tail-flick tests confirmed (Figures 8K, 8L) LHA-RVM connections primarily mediate the anti-nociceptive effects of $LHA_{post\text{-}dLS}$ neurons. The results observed from chemogenetic inhibition of RVMpost-LHA neurons were confirmed optogenetically and similar results were observed (Figures 8M-P). Recent observations indicate that the pro-nociceptive ON cells in the RVM can be either excitatory or inhibitory (Nguyen et al., 2022). Activating the excitatory ON cells results in hypersensitivity to noxious stimuli, whereas inhibiting the same neurons results in analgesia (Nguyen et al., 2022). Since the chemogenetic activation of the pro-nociceptive $RVM_{post\text{-}LHA}$ neurons resulted in thermal hyperalgesia and inhibition leading to pain suppression, we hypothesized that the $RVM_{post\text{-}LHA}$ neurons are excitatory. Thus, to test our hypothesis, we expressed Syn-GFP in the LHA of VGlut2-Cre mice, and PSD95-tagRFP in the RVM of the same mice (Figures S9A-D). When we visualized the RVM with confocal and super-resolution microscopy (Figure S9D), we found close apposition between the GFP-expressing pre-synaptic terminals and tagRFP-expressing VGlut2 expressing RVM neurons. Thus, we concluded that the excitatory LHA neurons impinge upon the excitatory RVM-ON neurons to facilitate RS-induced analgesia. The struggle to escape restraint engages dLS inhibitory neurons. The activated inhibitory dLS neurons silence excitatory $LHA_{post\text{-}dLS}$ neurons, which consequently disengages the pro-nociceptive $RVM_{post\text{-}LHA}$ neurons to drive RS-induced analgesia (Figure S9E, F).

Discussion

The dLS has been traditionally considered a key brain region for mediating stress responses (Anthony et al., 2014; Azevedo et al., 2020; Kubo et al., 2002; Singewald et al., 2011). However, the role of the dLS in SIA needs to be better understood. In this study, we have delineated the downstream partners of dLS and elucidated the mechanisms through which dLS neurons translate stress into pain suppression. We found that the dLS neurons are specifically geared towards coping with stress and, through their connections with the spinal cord via the LHA and the RVM, inhibit responses to noxious stimuli. In conclusion, our study has comprehensively evaluated the involvement of a key neural circuit in SIA by anatomically tracing their connections, monitoring, and manipulating neural activity.

We wondered what the etiologically relevant function of SIA might be, evolutionarily what benefits SIA might provide, and how dLS plays a role in it. SIA enables animals and humans to physiologically and behaviorally evade or cope with stressors in their immediate environment. When the perceived pain is attenuated, attention is drawn toward escaping the stressor. Several experiments support this view, including studies where rats were subjected to mild electric shocks from a floor plate in either an inescapable or an escapable chamber. It was observed that analgesia occurred when the rats could not escape the chamber after experiencing the electric shocks as opposed to when they could escape (Maier et al., 1982; Terman and Liebeskind, 1986). In line with these studies, we experimentally observed SIA only when mice were restrained for enough time (~1 hour) or when dLS neurons were activated for ~30 minutes (Figures S2C, D). We propose that acute restraint drives animals to attempt to escape, and during these attempts dLS neurons are engaged. When the dLS neurons are activated repeatedly, it provides a short-term analgesia.

SIA can be particularly pertinent in individuals with chronic pain, where pathological pain can impede the ability to react to a stressor on time. The role of dLS neurons in chronic pain is unclear. Interestingly, a recent study has shown that the dLS neurons promote both pain and anxiety (Wang et al., 2023). This is contrary to our data which shows that dLS activation has analgesic effects.

The contradiction may be since dLS neurons may play opposing roles under acute and chronic stress conditions. In contrast to acute stress, mechanisms of which we have explored here, chronic stress which Wang et al. studied, is known to exacerbate pain (Wang et al., 2023). In addition, the targeted coordinates for dLS used in the study are medial compared to the ones used in our study. However, as mentioned before, lesion studies in humans or animals have consistently indicated that dLS or medial septum stimulation is anti-nociceptive, irrespective of the nature of the noxious stimulus.

Early studies showed that SIA could either be opioid-dependent or independent (Watkins and Mayer, 1986). Naltrexone administration blocked SIA in rats who had undergone electric shocks (Drugan et al., 1981; Maier et al., 1980). Surprisingly, it was found that acute stress can sequentially induce both opioid dependent as well as opioid-independent SIA (Grau et al., 1981). Mutant mice without functional ß-endorphin (endogenous ligand for the mu-opioid receptor, OPRM1) lacked opioid-dependent SIA (mild swim stress), however, they displayed opioid-independent SIA (cold-swim stress) (Rubinstein et al., 1996). Interestingly, opioid-

dependent SIA was primarily induced when the animals underwent stress in inescapable chambers. Thus, successful induction of SIA may depend on the mode of stress delivery, and the opioid dependence may be decided by the exposure time. Our data too suggests that dLS-mediated RS-induced analgesia is opioid dependent, as we found that SIA induced by dLS activation is reversible by naltrexone administration (Figures S8A-C). Further, we show that RVM-ON cells play a critical role in dLS-mediated SIA. This observation is supported by a recent study that demonstrated the necessity of kappa-opioid receptors expressing RVM neurons in SIA (Nguyen et al., 2022). Together, the restraint-induced silencing of LHA excitatory neurons by dLS may turn downstream mu-opioid receptor-expressing RVM-ON cells amenable to enkephalin and endorphin-mediated modulation and consequent analgesia. Typically, RVM-ON cells target enkephalinergic and GABAergic spinal interneurons in the superficial layers of the dorsal horn that gate pain in turn through their connections with the somatosensory primary inputs to modulate pain (François et al., 2017). However, the neurons of our interest in the RVM target the deeper layers (V/VI) in the dorsal horn and may modulate nociceptive thresholds through independent mechanisms (Figure 6F). Interestingly, LHA is known to have direct spinal projections and thus can directly modulate pain bypassing RVM (Hancock, 1976), (Willis and Coggeshall, 2012). LHA neurons can modulate pain through direct orexinergic inputs to the spinal cord (van den Pol, 1999; Wang et al., 2018). The direct orexinergic LHA inputs to the spinal cord terminate in the superficial layers of the spinal cord. At the same time, the LHA neurons of our interest provide indirect inputs via RVM to the deeper layers of the spinal cord. Thus, two independent neural pathways (direct and indirect) originating from the LHA may mediate SIA. The orexinergic system housed in the LHA is recruited by acute stress and thus can supplement the LS-LHA-RVM-spinal cord circuitry in stress-induced pain modulation. We did not find direct inputs of $LHA_{post\text{-}dLS}$ neurons in the spinal cord with an AAV-mediated labeling strategy; however, these neurons can have partial overlap with the orexin population, and our method may not be sensitive enough to label the axon terminals in the spinal cord.

Notably, LHA neurons are known to respond to stress stimuli (Owens-French et al., 2022; Wang et al., 2021) and thus can cause SIA independently of dLS. The dLS independent SIA mechanisms might be driven by the direct orexinergic inputs to the spinal cord from LHA or the PV-expressing LHA neurons can mediate SIA through projections to the PAG (Siemian et al., 2021). This is reflected in our results where we observed transient activation of $LHA_{post\text{-}dLS}$ neurons when the mice struggled in the RS assay (Figure 5D). In addition to the excitatory projections tested here, there are inhibitory neurons in the LHA that project to the PBN (Moga et al., 1990). We primarily focused on the excitatory targets of dLS in the LHA, however, LHA is rich in GABAergic neurons and the potential roles of inhibitory targets of dLS in stress-responses remain to be tested. How both excitatory and inhibitory outputs from the LHA can modulate responses to noxious stimuli remains to be investigated. Decades of circuit tracing and functional anatomy studies have revealed synaptic targets of LHA across the brain, including the dLS (Cassidy et al., 2019). Such bidirectional connections also exist between the RVM and LHA and exploring the roles of recurrent connections between dLS-LHA/ LHA-RVM in stress-induced pain modulation will further delineate circuit mechanisms of SIA. We developed the microparticle-based CNO administration tool for projection-specific chronic DREADD ligand delivery. The same tool,

by tweaking the release rates of the CNO, can be effectively used for chronic neuronal activation/silencing. Finally, the mechanistic interrogation of dLS-centric SIA circuits has revealed a hypothalamic coordinate that effectively connects dLS with RVM to influence nociceptive thresholds. We have primarily focused on thermal nociceptive thresholds, however, it will be interesting to explore how dLS-LHA circuitry influences the effects of stress on other somatosensory modalities, such as itch.

Experimental Model and Subject Details

Animals

Animal care and experimental procedures were performed following protocols approved by the CPSCEA at the Indian Institute of Science. The animals were housed at the IISc Central Animal Facility under standard animal housing conditions: 12 h light/dark cycle from 7:00 am to 7:00 pm with ad libitum access to food and water, mice were housed in IVC cages in Specific pathogen-free (SPF) clean air rooms. Mice strains used: Vglut2-Cre or Vglut2-ires-Cre or Slc17a6tm2(Cre) Lowl/J(Stock number 016963); Ai14 (B6;129S6-Gt(ROSA)26Sortm9(CAG-tdTomato)Hze/J (Stock No 007905), BALB/cJ (Jackson Laboratories, USA). Experimental animals were between 2-4 months old.

Methods

Viral vectors and stereotaxic injections

Mice were anesthetized with 2% isoflurane/oxygen before and during the surgery. Craniotomy was performed at the marked point using a hand-held micro-drill (RWD, China). A Hamilton syringe (10 µL) with a glass pulled needle was used to infuse 300 nL of viral particles (1:1 in saline) at 100 nL/minute. The following coordinates were used to introduce virus/dyes: dLS- Anterior-Posterior (AP): +0.50, Medial-Lateral (ML): + 0.25; Dorsal-Ventral (DV): -2.50; LHA- AP: -1.70, ML: ±1.00; DV: -5.15; RVM- AP: -5.80, ML: +0.25; DV: -5.25; LPBN- AP: -5.34, ML: ±1.00, DV: -3.15. Vectors used and sources: ssAAV-9/2-hGAD67-chl-icre-SV40p(A) (University of Zurich, Catalog# v197-9), pAAV5-hsyn-DIO-EGFP (Addgene, Catalog# 50457-AAV 1), pAAV5-FLEX-tdTomato (Addgene, Catalog# 28306-PHP.S), pENN.AAV5.hSyn.TurboRFP.WPRE.RBG (Addgene, Catalog# 10552-AAV1), pAAV5-hsyn-DIO-hM3D(Gq)-mCherry (Addgene, Catalog# v141469), pAAV5-hsyn-DIO-hM4D(GI)-mCherry (Addgene, Catalog# 44362-AAV5), AAV9.syn.flex.GcaMP6s (Addgene, Catalog# pNM V3872TI-R(7.5)), pAAV-Ef1a-DIO-eNPHR 3.0-EYFP (Addgene, Catalog# v32533), pAAV-EF1a-double floxed-hChR2(H134R)-GFP-WPRE-HGHpA(Addgene, Catalog# v64219), AAV1-hSyn-Cre.WPRE.hGH (Addgene, Catalog# v126225), AAVretro-pmSyn1-EBFP-Cre (Donated by Ariel Levine, NIH), AAV retro-hSynapsin-Flpo (Donated by Ariel Levine, NIH), scAAV-1/2-hSyn1-FLPO-SV40p(A) (University of Zurich, Catalog# v59-1), ssAAV-1/2-shortCAG-(pre)mGRASP-WPRE-SV40p(A) (University of Zurich, Catalog# v653-1), ssAAV-1/2-fDIO-(post)mGRASP_2A_tdTomato(University of Zurich, Catalog# v651-1), pAAV-Ef1a-DIO-tdTomato (Addgene, Catalog# 28306-PHP.S), pAAV-hSyn-fDIO-hM3D(Gq)-mCherry-WPREpA (Addgene, Catalog# 154868-AAVrg), ssAAV-9/2-hSyn1-chl-dlox-EGFP_2A_FLAG_TeTxLC(rev)-dFRT-WPRE-hGHp(A) (University of Zurich, Catalog#

v322-9), AAVretro-hSyn-NLS-mCherry (Donated by Ariel Levine, NIH), AAV9-DIO-GephyrinTagRFP (Donated by Mark Hoon, NIH), AAV9-DIO-PSD95-TagRFP (Donated by Mark Hoon, NIH), AAV5-hSyn-DIO-mSyp1_EGFP(University of Zurich, Catalog# v484-9). For rabies tracing experiments, rAAV5-EF1α-DIO-oRVG (BrainVTA, Catalog# PT-0023) and rAAV5-EF1α-DIO-EGFP-T2A-TVA (BrainVTA, Catalog# PT-0062) were injected first, followed by RV-EnvA-Delta G-dsRed (BrainVTA, Catalog# R01002) after 2 weeks. Tissue was harvested after 1 week of rabies injection for histochemical analysis. Post-hoc histological examination of each injected mouse was used to confirm that viral-mediated expression was restricted to target nuclei.

Optogenetic and Photometry fiber implantation

Fiber optic cannula from RWD, China; Ø1.25 mm Ceramic Ferrule, 200 µm Core, 0.22 NA, L = 5 mm were implanted at AP: 0.50, ML: +0.25; DV: -2.50 in the dLS and L= 7 mm fibers were implanted at AP: -1.70, ML: ±1.00; DV: -5.15 in the LHA, and AP: -5.80, ML: +0.25; DV: -5.25 in the RVM after AAV carrying GCaMP6s, Channelrhodopsin2 or Halorhodopsin were infused. Animals were allowed to recover for at least 3 weeks before performing behavioral tests. Successful labeling and fiber implantation were confirmed post hoc by staining for GFP/mCherry for viral expression and injury caused by the fiber for implantation. Animals with viral-mediated gene expression at the intended locations and fiber implantations, as observed in post hoc tests, were only included.

Behavioral assays

Behavioral assays for the same cohorts were handled by a single experimenter. Prior to experimentation, the experimenter was blinded to the identity of animals. Mice were habituated in their home cages for at least 30 minutes in the behavior room before experiments. An equal male-to-female ratio was maintained in every experimental cohort and condition unless otherwise stated, with no significant differences seen between sexes in the responses recorded from the behavioral experiments. Wherever possible, efforts were made to keep the usage of animals to the minimum. Deschloroclozapine (DCZ) was diluted in saline (final concentration: 0.1 mg/kg) and injected intraperitoneal (i.p.) 15-20 minutes before behavioral experiments or histochemical analysis. Mice were injected with intra-plantar (i.pl.) Complete Freund's adjuvant (CFA) one day before the behavioral experiments to cause persistent inflammatory pain and thermal hypersensitivity. All the experiments were videotaped simultaneously with three wired cameras (Logitech, USA) placed horizontally and scored offline post hoc manually. The programmable hot plate with gradient function and tail flick analgesiometer (Orchid Scientific, India) were used according to the manufacturer's instructions. For optogenetic stimulations fiber-coupled laser (channelrhodopsin activation; RWD, China), fiber-coupled LEDs (for halorhodopsin stimulation; Prizmatix, Israel) were used. Prior to the behavioral testing the optic fibers were connected to the cannulae implanted in the mice brain. The animals were habituated for 30 minutes prior to the commencement of the experiments. The light-dark box tracking and estimations of the time-spent in either chamber were carried out with DeepLabCut and the data were trained and analyzed on a custom-built computer system with AMD Ryzen 9 5900x 12-core processor 24 with NVIDIA Corporation Graphics Processing Unit (GPU) (Mathis et al., 2018), (Nath et al., 2019) .

The RS assay was used to induce stress in the experiments reported here. In short, mice were restrained for one hour in a ventilated falcon tube, followed by testing them for stress-related and noxious behaviors using the Light Dark Box Assay, the Hot Plate Assay, and the Tail Flick Assay.

Blood corticosterone levels were measured using the Mouse corticosterone Enzyme-linked immunosorbent assay (ELISA) kit (BIOLABS, USA) by collecting blood from wild-type mice, wild-type mice subjected to RS, and dLSGad67-hM3Dq mice administered with DCZ. Plasma extracted from each of the collected blood samples were subjected to Competitive ELISA. Wells pre-coated with corticosterone antigen were incubated with the respective sample in triplicates. Biotin-conjugated primary antibody was added, followed by incubation with streptavidin-horseradish peroxidase (HRP). Finally, the samples turned from yellow to blue in color depending on the concentration of corticosterone present in the sample when Tetramethylbenzidine (TMB) substrate was added. The optical density (O.D.)of the samples was recorded using a spectrophotometer.

The mice were subjected to four primary behavioral assays for the fiber photometry experiments. In the immobilization experiments, experimenter physically restrained the mice by pressing them down by hand for approximately 10 seconds. In the tail hanging experiments, the mice were suspended upside down by their tail for 10 seconds. In the RS assay, photometry signals were recorded through the fiber coupled cannulae that passed through a modified RS-inducing falcon tube to allow unrestricted recording. On the hot plate test the mice were acclimatized to the equipment with the optic fiber connected to the cannulae a day before experimentations. During the experiments, the equipment was first allowed to reach the desired temperature and then the animals were introduced on the hot-plate test.

The collected photometry data was minimally processed with autofluorescence (405 nm) background subtraction and within trial fluorescence normalization. The median value of data points within the 10 minutes of home-cage recordings prior initiation of RS or thermal-plate experiments was used as the normalization factor. Z -score transformation of the fluorescence data was performed with the RWD in-built software.

Immunostaining, multiplex in situ hybridization, and confocal microscopy

Mice were anesthetized with isoflurane and perfused intracardially with 1X Phosphate Buffered Saline (PBS) (Takara, Japan) and 4% Paraformaldehyde (PFA) (Ted Pella, Inc., USA), consecutively for immunostaining experiments. Fresh brains were harvested for in situ hybridization experiments. For the cFos experiments, brains were harvested 90 minutes after RS assay, and 150 minutes after i.p. clozapine N-Oxide (CNO) administration. Tissue sections were rinsed in 1X PBS and incubated in a blocking buffer (2% Bovine Serum Albumin (BSA); 0.3% Triton X-100; PBS) for 1 hour at room temperature. Sections were incubated in primary antibodies in blocking buffer at room temperature overnight. Sections were rinsed 1-2 times with PBS and incubated for 2 hours in Alexa Fluor conjugated goat anti-rabbit/ chicken or donkey anti-goat/rabbit secondary antibodies (Invitrogen) at room temperature, washed in PBS, and mounted in VectaMount permanent mounting media (Vector Laboratories Inc.) onto charged glass slides (Globe Scientific Inc.). Multiplex in-situ hybridization (ISH) was done with a manual RNAscope assay (Advanced Cell Diagnostics,

USA). Probes were ordered from the ACD online catalogue. We used an upright fluorescence microscope (Khush, Bengaluru) (2.5X, 4X, and 10X lenses) and ImageJ/FIJI image processing software to image, and process images for the verification of anatomical location of cannulae implants. For the anatomical studies the images were collected with 10X and 20X objective on a laser scanning confocal system (Leica SP8 Falcon, Germany) and processed using the Leica image analysis suite. For the Airy Scan Imaging, Zeiss 980 was used (NCBS Central Imaging Core facility).

CUBIC clearing and imaging

In order to visualize the fluorescent neuronal labeling in the cleared brain tissue, 300 µm thick sections were cleared by first washing with 1X PBS for 30 minutes, followed by 2 hour incubation in 50% Cubic L (TCI, Japan)solution (Susaki et al., 2020). Next, the sections were immersed and incubated in 100% Cubic L solution overnight at 37°C. The sections were preserved and imaged in the Cubic R+ (TCI, Japan) solution. For imaging the cleared sections, 10X and 20X objectives were used along with the Leica SP8 Confocal microscope.

CNO Encapsulation

CNO was encapsulated within poly-lactic-*co*-glycolic acid (PLGA, M_w 10–15 kDa, LG 50:50, PolySciTech, IN, USA) microparticles using a single emulsion method. Briefly, 100 mg PLGA and 2 mg CNO were dissolved in 1 mL dichloromethane (DCM) and mixed for 10 minutes. This mixture was homogenized (IKA® T18 digital Ultra Turrax) with 10 mL 1% polyvinyl alcohol (PVA) at 12000 rpm, resulting in an emulsion. This emulsion was added to 100 mL 1% PVA with magnetic stirring to allow DCM to evaporate. After 4 hours, the microparticles were collected by centrifugation (8000 *g*) and washed thrice with deionized water to remove PVA. The suspension was frozen, followed by lyophilization to obtain the CNO-encapsulated microparticles as powder. For experiments, the powder was weighed and resuspended in 1X PBS to get a concentration of 0.5 mg/mL.

Quantification and Statistical Analysis

All statistical analyses (t-test and one way ANOVA test) were performed using GraphPad PRISM 8.0.2 software. ns > 0.05, $*$ $P \leq 0.05$, $**$ $P \leq 0.01$, $***$ $P \leq 0.001$, $****$ $P \leq 0.0005$.

Data availability

Raw data will be made available upon request.

Acknowledgements

We thank Annappa for providing animal care and facilitating behavioral experiments. We thank the Central Animal Facility for supporting animal experiments. We thank the central bioimaging facilities at IISc for confocal microscopy, and at NCBS, Bengaluru for Airy scan imaging. We thank DST-FIST program for funding the animal behavioral facility at the Center for Neuroscience.

Funding
We thank the DST-SERB CRG, IndiaAlliance Intermediate Fellowship, and IISc Bengaluru for funding our research.

Competing interests
The authors report no competing interests.

References

Abbott FV, Melzack R. 1978. Analgesia produced by stimulation of limbic structures and its relation to epileptiform after-discharges. *Exp Neurol* **62**:720–734.

Albert DJ, Wong RC. 1978. Hyperreactivity, muricide, and intraspecific aggression in the rat produced by infusion of local anaesthetic into the lateral septum or surrounding areas. *Journal of Comparative and Physiological Psychology*. doi:10.1037/h0077524

Alexander GM, Rogan SC, Abbas AI, Armbruster BN, Pei Y, Allen JA, Nonneman RJ, Hartmann J, Moy SS, Nicolelis MA, McNamara JO, Roth BL. 2009. Remote control of neuronal activity in transgenic mice expressing evolved G protein-coupled receptors. *Neuron* **63**:27–39.

Alteration in footshock threshold by low-level septal brain stimulation. 1970. . *Physiol Behav* **5**:715–719.

Amit Z, Galina ZH. 1986. Stress-induced analgesia: adaptive pain suppression. *Physiol Rev* **66**:1091–1120.

Anthony TE, Dee N, Bernard A, Lerchner W, Heintz N, Anderson DJ. 2014. Control of stress-induced persistent anxiety by an extra-amygdala septohypothalamic circuit. *Cell* **156**:522–536.

Arthurs JW, Pauli JL, Palmiter RD. 2023. Activation of Parabrachial Tachykinin 1 Neurons Counteracts Some Behaviors Mediated by Parabrachial Calcitonin Gene-related Peptide Neurons. *Neuroscience* **517**:105–116.

Azevedo EP, Tan B, Pomeranz LE, Ivan V, Fetcho R, Schneeberger M, Doerig KR, Liston C, Friedman JM, Stern SA. 2020. A limbic circuit selectively links active escape to food suppression. *Elife* **9**. doi:10.7554/eLife.58894

Barik A, Thompson JH, Seltzer M, Ghitani N, Chesler AT. 2018. A Brainstem-Spinal Circuit Controlling Nocifensive Behavior. *Neuron* **100**:1491–1503.e3.

Behbehani MM, Park MR, Clement ME. 1988. Interactions between the lateral hypothalamus and the periaqueductal gray. *J Neurosci* **8**:2780–2787.

Benabid AL, Jeaugey L. 1989. Cells of the rat lateral habenula respond to high-threshold somatosensory inputs. *Neurosci Lett* **96**:289–294.

Brady JV, Nauta WJ. 1955. Subcortical mechanisms in emotional behavior: the duration of affective changes following septal and habenular lesions in the albino rat. *J Comp Physiol Psychol* **48**:412–420.

Brady JV, Nauta WJ. 1953. Subcortical mechanisms in emotional behavior: affective changes following septal forebrain lesions in the albino rat. *J Comp Physiol Psychol* **46**:339–346.

Butler RK, Finn DP. 2009. Stress-induced analgesia. *Prog Neurobiol* **88**:184–202.

Callaway EM, Luo L. 2015. Monosynaptic Circuit Tracing with Glycoprotein-Deleted Rabies Viruses. *J Neurosci* **35**:8979–8985.

Campbell EJ, Marchant NJ. 2018. The use of chemogenetics in behavioural neuroscience: receptor variants, targeting approaches and caveats. *Br J Pharmacol* **175**:994–1003.

Campos CA, Bowen AJ, Roman CW, Palmiter RD. 2018. Encoding of danger by parabrachial CGRP neurons. *Nature* **555**:617–622.

Carr KD, Uysal S. 1985. Evidence of a supraspinal opioid analgesic mechanism engaged by lateral hypothalamic electrical stimulation. *Brain Res* **335**:55–62.

Cassidy RM, Lu Y, Jere M, Tian J-B, Xu Y, Mangieri LR, Felix-Okoroji B, Selever J, Xu Y, Arenkiel BR, Tong Q. 2019. A lateral hypothalamus to basal forebrain neurocircuit promotes feeding by suppressing responses to anxiogenic environmental cues. *Sci Adv* **5**:eaav1640.

Chen T-W, Wardill TJ, Sun Y, Pulver SR, Renninger SL, Baohan A, Schreiter ER, Kerr RA, Orger MB, Jayaraman V, Looger LL, Svoboda K, Kim DS. 2013. Ultrasensitive

fluorescent proteins for imaging neuronal activity. *Nature* **499**:295–300.
Chiang MC, Nguyen EK, Canto-Bustos M, Papale AE, Oswald A-MM, Ross SE. 2020. Divergent Neural Pathways Emanating from the Lateral Parabrachial Nucleus Mediate Distinct Components of the Pain Response. *Neuron* **106**:927–939.e5.
Cohen SR, Melzack R. 1985. Morphine injected into the habenula and dorsal posteromedial thalamus produces analgesia in the formalin test. *Brain Res* **359**:131–139.
Dafny N, Dong WQ, Prieto-Gomez C, Reyes-Vazquez C, Stanford J, Qiao JT. 1996. Lateral hypothalamus: site involved in pain modulation. *Neuroscience* **70**:449–460.
Drugan RC, Grau JW, Maier SF, Madden J 4th, Barchas JD. 1981. Cross tolerance between morphine and the long-term analgesic reaction to inescapable shock. *Pharmacol Biochem Behav* **14**:677–682.
Fields H. 2004. State-dependent opioid control of pain. *Nat Rev Neurosci* **5**:565–575.
Fields HL, Heinricher MM, Mason P. 1991. Neurotransmitters in nociceptive modulatory circuits. *Annu Rev Neurosci* **14**:219–245.
Fields HL, Malick A, Burstein R. 1995. Dorsal horn projection targets of ON and OFF cells in the rostral ventromedial medulla. *Journal of Neurophysiology*. doi:10.1152/jn.1995.74.4.1742
Finn D. 2017. The impact of stress on pain. *Physiology News*. doi:10.36866/pn.108.25
Franco AC, Prado WA. 1996. Antinociceptive effects of stimulation of discrete sites in the rat hypothalamus: evidence for the participation of the lateral hypothalamus area in descending pain suppression mechanisms. *Braz J Med Biol Res* **29**:1531–1541.
François A, Low SA, Sypek EI, Christensen AJ, Sotoudeh C, Beier KT, Ramakrishnan C, Ritola KD, Sharif-Naeini R, Deisseroth K, Delp SL, Malenka RC, Luo L, Hantman AW, Scherrer G. 2017. A Brainstem-Spinal Cord Inhibitory Circuit for Mechanical Pain Modulation by GABA and Enkephalins. *Neuron* **93**:822–839.e6.
Fuchs PN, Melzack R. 1995. Analgesia induced by morphine microinjection into the lateral hypothalamus of the rat. *Exp Neurol* **134**:277–280.
Gol A. 1967. Relief of pain by electrical stimulation of the septal area. *Journal of the Neurological Sciences*. doi:10.1016/0022-510x(67)90012-3
Grau JW, Hyson RL, Maier SF, Madden J 4th, Barchas JD. 1981. Long-term stress-induced analgesia and activation of the opiate system. *Science* **213**:1409–1411.
Hancock MB. 1976. Cells of origin of hypothalamo-spinal projections in the rat. *Neurosci Lett* **3**:179–184.
Han S, Soleiman MT, Soden ME, Zweifel LS, Palmiter RD. 2015. Elucidating an Affective Pain Circuit that Creates a Threat Memory. *Cell* **162**:363–374.
Holden JE, Pizzi JA. 2008. Lateral hypothalamic-induced antinociception may be mediated by a substance P connection with the rostral ventromedial medulla. *Brain Res* **1214**:40–49.
Jain RA. 2000. The manufacturing techniques of various drug loaded biodegradable poly(lactide-co-glycolide) (PLGA) devices. *Biomaterials* **21**:2475–2490.
Kim J, Zhao T, Petralia RS, Yu Y, Peng H, Myers E, Magee JC. 2011. mGRASP enables mapping mammalian synaptic connectivity with light microscopy. *Nat Methods* **9**:96–102.
Köhler C. 1976. Habituation of the orienting response after medial and lateral septal lesions in the albino rat. *Behav Biol* **16**:63–72.
Kubo T, Kanaya T, Numakura H, Okajima H, Hagiwara Y, Fukumori R. 2002. The lateral septal area is involved in mediation of immobilization stress-induced blood pressure increase in rats. *Neurosci Lett* **318**:25–28.
Lerner TN, Shilyansky C, Davidson TJ, Evans KE, Beier KT, Zalocusky KA, Crow AK, Malenka RC, Luo L, Tomer R, Deisseroth K. 2015. Intact-Brain Analyses Reveal

Distinct Information Carried by SNc Dopamine Subcircuits. *Cell* **162**:635–647.
Lewis JW, Sherman JE, Liebeskind JC. 1981. Opioid and non-opioid stress analgesia: assessment of tolerance and cross-tolerance with morphine. *J Neurosci* **1**:358–363.
Mahieux G, Benabid AL. 1987. Naloxone-reversible analgesia induced by electrical stimulation of the habenula in the rat. *Brain Res* **406**:118–129.
Maier SF, Davies S, Grau JW, Jackson RL, Morrison DH, Moye T, Madden J 4th, Barchas JD. 1980. Opiate antagonists and long-term analgesic reaction induced by inescapable shock in rats. *J Comp Physiol Psychol* **94**:1172–1183.
Maier SF, Drugan RC, Grau JW. 1982. Controllability, coping behavior, and stress-induced analgesia in the rat. *Pain* **12**:47–56.
Ma QP, Shi YS, Han JS. 1992. Further studies on interactions between periaqueductal gray, nucleus accumbens and habenula in antinociception. *Brain Res* **583**:292–295.
Mathis A, Mamidanna P, Cury KM, Abe T, Murthy VN, Mathis MW, Bethge M. 2018. DeepLabCut: markerless pose estimation of user-defined body parts with deep learning. *Nat Neurosci* **21**:1281–1289.
Moga MM, Saper CB, Gray TS. 1990. Neuropeptide organization of the hypothalamic projection to the parabrachial nucleus in the rat. *The Journal of Comparative Neurology*. doi:10.1002/cne.902950409
Nagai Y, Miyakawa N, Takuwa H, Hori Y, Oyama K, Ji B, Takahashi M, Huang X-P, Slocum ST, DiBerto JF, Xiong Y, Urushihata T, Hirabayashi T, Fujimoto A, Mimura K, English JG, Liu J, Inoue K-I, Kumata K, Seki C, Ono M, Shimojo M, Zhang M-R, Tomita Y, Nakahara J, Suhara T, Takada M, Higuchi M, Jin J, Roth BL, Minamimoto T. 2020. Deschloroclozapine, a potent and selective chemogenetic actuator enables rapid neuronal and behavioral modulations in mice and monkeys. *Nat Neurosci* **23**:1157–1167.
Nath T, Mathis A, Chen AC, Patel A, Bethge M, Mathis MW. 2019. Using DeepLabCut for 3D markerless pose estimation across species and behaviors. *Nat Protoc* **14**:2152–2176.
Nguyen E, Smith KM, Cramer N, Holland RA, Bleimeister IH, Flores-Felix K, Silberberg H, Keller A, Le Pichon CE, Ross SE. 2022. Medullary kappa-opioid receptor neurons inhibit pain and itch through a descending circuit. *Brain* **145**:2586–2601.
Olds J, Milner P. 1954. Positive reinforcement produced by electrical stimulation of septal area and other regions of rat brain. *J Comp Physiol Psychol* **47**:419–427.
Owens-French J, Li S-B, Francois M, Leigh Townsend R, Daniel M, Soulier H, Turner A, de Lecea L, Münzberg H, Morrison C, Qualls-Creekmore E. 2022. Lateral hypothalamic galanin neurons are activated by stress and blunt anxiety-like behavior in mice. *Behav Brain Res* **423**:113773.
Rizzi-Wise CA, Wang DV. 2021. Putting Together Pieces of the Lateral Septum: Multifaceted Functions and Its Neural Pathways. *eNeuro* **8**. doi:10.1523/ENEURO.0315-21.2021
Rubinstein M, Mogil JS, Japón M, Chan EC, Allen RG, Low MJ. 1996. Absence of opioid stress-induced analgesia in mice lacking beta-endorphin by site-directed mutagenesis. *Proc Natl Acad Sci U S A* **93**:3995–4000.
Sharma PR, Dravid AA, Kalapala YC, Gupta VK, Jeyasankar S, Goswami A, Agarwal R. 2022. Cationic inhalable particles for enhanced drug delivery to M. tuberculosis infected macrophages. *Biomaterials Advances*. doi:10.1016/j.msec.2021.112612
Sheehan TP, Chambers RA, Russell DS. 2004. Regulation of affect by the lateral septum: implications for neuropsychiatry. *Brain Res Brain Res Rev* **46**:71–117.
Shelton L, Becerra L, Borsook D. 2012. Unmasking the mysteries of the habenula in pain and analgesia. *Prog Neurobiol* **96**:208–219.
Siemian JN, Arenivar MA, Sarsfield S, Borja CB, Erbaugh LJ, Eagle AL, Robison AJ,

Leinninger G, Aponte Y. 2021. An excitatory lateral hypothalamic circuit orchestrating pain behaviors in mice. *Elife* **10**. doi:10.7554/eLife.66446
Singewald GM, Rjabokon A, Singewald N, Ebner K. 2011. The modulatory role of the lateral septum on neuroendocrine and behavioral stress responses. *Neuropsychopharmacology* **36**:793–804.
Stachniak TJ, Ghosh A, Sternson SM. 2014. Chemogenetic synaptic silencing of neural circuits localizes a hypothalamus→midbrain pathway for feeding behavior. *Neuron* **82**:797–808.
Susaki EA, Shimizu C, Kuno A, Tainaka K, Li X, Nishi K, Morishima K, Ono H, Ode KL, Saeki Y, Miyamichi K, Isa K, Yokoyama C, Kitaura H, Ikemura M, Ushiku T, Shimizu Y, Saito T, Saido TC, Fukayama M, Onoe H, Touhara K, Isa T, Kakita A, Shibayama M, Ueda HR. 2020. Versatile whole-organ/body staining and imaging based on electrolyte-gel properties of biological tissues. *Nat Commun* **11**:1982.
Terman GW, Liebeskind JC. 1986. Relation of stress-induced analgesia to stimulation-produced analgesia. *Ann N Y Acad Sci* **467**:300–308.
Terrill SJ, Maske CB, Williams DL. 2018. Endogenous GLP-1 in lateral septum contributes to stress-induced hypophagia. *Physiol Behav* **192**:17–22.
Todd AJ. 2010. Neuronal circuitry for pain processing in the dorsal horn. *Nat Rev Neurosci* **11**:823–836.
Tracey I, Mantyh PW. 2007. The cerebral signature for pain perception and its modulation. *Neuron* **55**:377–391.
Vaccarino AL, Marek P, Sternberg W, Liebeskind JC. 1992. NMDA receptor antagonist MK-801 blocks non-opioid stress-induced analgesia in the formalin test. *Pain* **50**:119–123.
van den Pol AN. 1999. Hypothalamic hypocretin (orexin): robust innervation of the spinal cord. *J Neurosci* **19**:3171–3182.
Wang C, Fujita T, Kumamoto E. 2018. Orexin B Modulates Spontaneous Excitatory and Inhibitory Transmission in Lamina II Neurons of Adult Rat Spinal Cord. *Neuroscience* **383**:114–128.
Wang D, Li A, Dong K, Li H, Guo Y, Zhang X, Cai M, Li H, Zhao G, Yang Q. 2021. Lateral hypothalamus orexinergic inputs to lateral habenula modulate maladaptation after social defeat stress. *Neurobiol Stress* **14**:100298.
Wang D, Pan X, Zhou Y, Wu Z, Ren K, Liu H, Huang C, Yu Y, He T, Zhang X, Yang L, Zhang H, Han M-H, Liu C, Cao J-L, Yang C. 2023. Lateral septum-lateral hypothalamus circuit dysfunction in comorbid pain and anxiety. *Mol Psychiatry*. doi:10.1038/s41380-022-01922-y
Watkins LR, Mayer DJ. 1986. Multiple Endogenous Opiate and Non-Opiate Analgesia Systems: Evidence of Their Existence and Clinical Implications. *Annals of the New York Academy of Sciences*. doi:10.1111/j.1749-6632.1986.tb14635.x
Wickersham IR, Finke S, Conzelmann K-K, Callaway EM. 2007. Retrograde neuronal tracing with a deletion-mutant rabies virus. *Nat Methods* **4**:47–49.
Willis WD Jr, Coggeshall RE. 2012. Sensory Mechanisms of the Spinal Cord: Volume 1 Primary Afferent Neurons and the Spinal Dorsal Horn. Springer Science & Business Media.
Xu W, Morishita W, Buckmaster PS, Pang ZP, Malenka RC, Südhof TC. 2012. Distinct neuronal coding schemes in memory revealed by selective erasure of fast synchronous synaptic transmission. *Neuron* **73**:990–1001.

Figure legends

Figure 1. dLS neurons are both sufficient and necessary for causing acute restraint-induced analgesia. (A) Schematic representing the Restraint Stress (RS) assay used to induce stress in mice. (B) cFos expression in the dLS of restrained mice compared to unrestrained control mice (Green-cFos, Red-neurotrace (nuclear dye specific to neuronal nuclei)). (C) Total number of cFos+ cells in the dLS (area marked by dotted lines) in restrained vs unrestrained mice (6.40±1.21 compared to 56.40±3.09, respectively; t-test, ***P=0.0001, n=5). (D) Multiplex In Situ hybridization with VGlut2 and VGat (red-VGat, green-VGlut2), highlighted by arrowheads (left), with zoom-in view of a rare VGlut2+ (green) cell (right). (E) Gad67-Cre and DIO-hM3Dq-mCherry/DIO-tdTomato were injected in the dLS of wild-type mice. (F) i.p. DCZ and not Saline evoked cFos expression (green) in the mCherry-positive cells (red) in the dLSGad67-hM3Dq neurons. (G) Tail-flick latency (seconds) (2.28±0.16 compared to 2.8±0.16, respectively; t-test, **P=0.0056, n=7) post-saline or DCZ administration in dLSGad67-hM3Dq mice, with no significant difference in dLSGad67-tdTomato mice. (H) Licks (8.71±1.76 compared to 4.14±0.74, respectively; t-test, *P=0.0335, n=7), and latency to lick (seconds) (15.57±2.03 compared to 22.86±2.26, respectively; t-test, *P=0.0338, n=7) on the hot-plate test of dLSGad67-tdTomato mice, administered with either i.p. Saline or DCZ, with no significant difference in dLSGad67-tdTomato mice. (I) Gad67-Cre and DIO-Tettox-GFP/DIO-GFP were co-injected in the dLS of wild-type mice. (J) GFP-positive neurons (green) seen in the dLS. (K) Tail-flick latency (seconds) (2.08±0.14 compared to 3.9±0.15, respectively; t-test, ***P=0.0001, n=8) with and without restraint for 1 hour using the RS assay in dLSGad67-GFPmice, with no significant difference in dLSGad67-Tettox-GFP mice. (L) Number of licks (8.57±1.34 compared to 4.57±0.69, respectively; t-test, **P=0.0089, n=7), and latency to lick (seconds) (14.29±1.54 compared to 24.14±1.40, respectively; t-test, ***P=0.0001, n=7) with and without restraint in dLSGad67-GFPmice, with no significant difference in dLSGad67-Tettox-GFP mice.

Figure 2. dLS neurons are engaged by acute stress due to physical restraint. (A) AAVs encoding Gad67-Cre and DIO-GCaMP6s were co-injected in the dLS, and fiber optic cannulaes were implanted above for recording neural activity. (B) Confirmation of the expression of GCaMP6s (Green) in the dLS neurons. (C) Schematic representation of the fiber photometry system. (D) Representative trace or neural activity from GCaMP6s (green) vs control GFP (blue) mice in the homecage. (E) Neural activity from the dLS while mice were under restraint. (F) Traces of neural activity when mice were allowed to move freely in the homecage (blue), and when they were under restraint (red). Peaks corresponding to neural activity (blue dashes) were seen when mice struggled in the tube. (G) Heatmap depicting neural activity during individual instances of struggles (initiation of struggle indicated by white dotted line). (H and I) Average plots and heatmaps for dLS responses on the hot plate at 32 deg (5 mice, 20 trials; dotted line indicating time point when mice were placed on the hotplate). (J and K) Average plots and heatmaps for dLS engagement on the hot plate at a noxious temperature of 52 deg (5 mice, 20 trials; dotted line indicating time point when mice were placed on the hotplate).

Figure 3. dLS neurons synapse onto a small neuronal population of LHA neurons. (A) Gad67-Cre and DIO-GFP injected in the dLS of wild-type mice. (B) GFP-positive cells seen in the dLS. (C) GFP-positive terminals from the dLS were seen in the Hippocampus (Hipp), Habenula (Hb) and Lateral Hypothalamus (LHA), marked region on LHA zoomed-in on the bottom. (D) Gad67-Cre and DIO-ChR2-YFP injected in the dLS of wild-type mice to express the excitatory opsin ChR2 in the dLSGad67 neurons. The fiber was implanted in the LHA to facilitate terminal activation. ChR2-YFP-positive terminals were observed in the LHA. (E) Tail-flick latency (seconds) (2.49±0.04 compared to 2.30±0.03, respectively; t-test, ***P=0.0001, n=7) with (ON) and without (OFF) blue light illumination in dLSGad67-ChR2 mice (F) Licks (12.86±1.50 compared to 5.57±0.75, respectively; t-test, ***P=0.001, n=7), and latency to lick (seconds) (12.43±0.72 compared to 22.29±1.34, respectively; t-test, ***P=0.0002, n=7) on the hot plate with (ON) and without (OFF) blue light illumination in dLSGad67-ChR2 mice. (G) AAVRetro-Cre was injected in the LHA and DIO-hM3Dq-mCherry/DIO-tdTomato in the dLS of wild-type mice. Presence of mCherry-positive cells (red) co-localised with cFos-positive cells (green) in the dLS (overlap between red and green cells shown in zoom-in box). (H) Tail-flick latency (seconds) (2.58±0.12 compared to 3.32±0.10, respectively; t-test, ***P=0.0005, n=7) post saline or DCZ administration in $dLS_{pre\text{-}LHA}$Gad67-hM3Dqmice, with no significant difference seen in $dLS_{pre\text{-}LHA}$Gad67-tdTomato mice. (I) Number of licks (11.14±1.45 compared to 6.29±0.89, respectively; t-test, *P=0.0147, n=7), and latency to lick (seconds) (11.29±1.51 compared to 16.43±1.39, respectively; t-test, *P=0.0277, n=7) post saline or DCZ administration in $dLS_{pre\text{-}LHA}$Gad67-hM3Dq mice.. (J) AAVTransyn-Cre injected in the dLS and DIO-hM3Dq-mCherry/DIO-tdTomato in the LHA of wild-type mice. Presence of mCherry-positive cells (red) co-localised with cFos-positive cells (green) in the LHA. (K) Tail-flick latency (seconds) (2.97±0.07 compared to 4.12±0.22, respectively; t-test, ***P=0.0003, n=7) post saline or DCZ administration in $LHA_{post\text{-}dLS}$hM3Dq mice, with no significant difference seen in $dLS_{post\text{-}dLS}$Gad67-tdTomato mice. (L) Number of licks (4.71±0.94 compared to 10.00±1.60, respectively; t-test, *P=0.0149, n=7), and latency to lick (seconds) (23.00±3.11 compared to 9.43±1.93, respectively; t-test, **P=0.003, n=7) post saline or DCZ administration $LHA_{post\text{-}dLS}$tdTomato mice, with no significant difference seen in $dLS_{post\text{-}dLS}$Gad67-tdTomato mice. (M) AAVTransyn-Cre injected in the dLS and DIO-hM3Dq-mCherry in the Habenula (Hb) of wild-type mice to express the excitatory DREADD. Presence of mCherry-positive cells (red) in the Hb. (N) Tail-flick latency post saline or DCZ administration in $Hb_{post\text{-}dLS}$hM3Dq mice. (O) Number and latency of licks (in seconds) post saline or DCZ administration in $Hb_{post\text{-}dLS}$hM3Dq mice. (P) AAVTransyn-Cre injected in the dLS and DIO-Tettox-GFP/DIO-GFP bilaterally in the LH of wild-type mice. Presence of GFP-positive cells (green) in the LHA. (Q) Tail-flick latency (seconds) (2.38±0.04 compared to 3.00±0.04, respectively; t-test, ***P=0.0001, n=7) with and without restraint in $LHA_{post\text{-}dLS}$GFP mice, with no significant difference seen in $LHA_{post\text{-}dLS}$TetTox mice. (R) Number of licks (9.43±0.92 compared to 4.00±0.53, respectively; t-test, ***P=0.0003, n=7), and latency to lick (seconds) (13.29±0.89 compared to 24.86±3.47, respectively; t-test, **P=0.0072, n=7) with and without restraint in $LHA_{post\text{-}dLS}$GFP mice, with no significant difference seen in $LHA_{post\text{-}dLS}$TetTox mice.

Figure 4: $LHA_{post\text{-}dLS}$ neurons are glutamatergic in nature. (A) AAV encoding Transsyn-FlpO injected in the dLS; fDIO-tdTomato, and DIO-GFP injected in the LHA of VGlut2-Cre transgenic mice. (B) Overlapping red and green cells (yellow, seen in the zoom-in box marked by arrowheads) were seen in the LHA. (C) AAVTransyn-Cre injected in the dLS of Ai14 transgenic mice. (D) The LHA was labeled with probes against VGlut2 using in situ hybridization. Co-localisation of tdTomato-positive (red) and GFP-positive (green) cells in the LHA (overlapping areas marked by arrowheads), zoom-in of overlap on right. (E) AAVs encoding Gad67-Cre and DIO-Synaptophysin-GFP injected in the dLS and DIO Gephyrin-tagRFP in the LHA of VGlut2-Cre transgenic mice. (F) Closely apposed green synaptophysin and red gephyrin puncta seen in the LHA (zoom-in of overlap on right).

Figure 5. $LHA_{post\text{-}dLS}$ neurons are acutely engaged during the initial struggle due to physical restraint. (A) AAVTransyn-Cre injected in the dLS and DIO-GCaMP6s in the LHA of wild-type mice to record neural activity from the $LHA_{post\text{-}dLS}$ neurons. (B) GCaMP6s-positive cells (green) and tissue injury from the fiber implant seen in the LHA, zoom-in of the marked area on the right. (C) Sample trace of neural activity when mice were allowed to move freely in the homecage (blue), and when they were under restraint (red). Peaks corresponding to neural activity (blue dashes) were seen when mice struggled in the tube. (D) Cumulative plots for calcium transients when mice struggled under restraint (5mice, 12 trials)**.** (E) Heat maps depicting neural activity in $LHA_{post\text{-}dLS}$ (left) and dLSGad67 neurons (right) during struggle in the RS assay (5 mice, 12 trials; dotted lines indicating initiation of struggle in RS assay).

Figure 6. RVM ON-cells are downstream of the dLS→LHA circuitry. (A) AAVTransyn-Cre injected in the dLS and DIO-GFP in the LHA of wild-type mice to label the $LHA_{post\text{-}dLS}$ neurons. (B) GFP-positive cell bodies in the LHA (green, left; zoom-in of LHA in the box on bottom). Projections of the $LH_{post\text{-}dLS}$ neurons in the PBN, and RVM. (C) Presence of fluorescence (black) in RVM post tissue clearing of the same brains expressing GFP in the $LHA_{post\text{-}dLS}$neurons. (D) AAVTransyn-Cre injected in the LHA and DIO-GFP in the RVM of wild-type mice to label the $RVM_{post\text{-}LHA}$ neurons with GFP. (E) GFP-positive cell bodies (black, marked by arrowheads) seen in the RVM. (F) Projections from the $RVM_{post\text{-}LHA}$ were observed in the lumbar spinal cord. (G) AAVTransyn-Cre injected in the dLS, and DIO-G and DIO-TVA-GFP in the LHA of wild-type mice. Three weeks later, the delG-Rabies-mCherry virus was injected into the RVM. (H) Starter cells (yellow) observed in the LHA. mCherry-positive cell bodies (red) seen in the dLS (marked region zoomed-in on the right with overlapping cells marked with arrowheads). (I) AAVRetro-FlpO injected in the RVM, fDIO-post-GRASP injected in the LHA, and Pre-GRASP in the dLS of wild-type mice. (J) Axon terminals from the dLS neurons (Green) were observed around the $LHA_{pre\text{-}RVM}$ (red) cell-bodies (zoom-in of overlaps on the right).

Figure 7. $RVM_{post\text{-}LHA}$ neurons fire during nocifensive behaviors on the hotplate and respond to RS-mediated struggle. (A) AAVTransyn-Cre was injected in the LHA with DIO-GCaMP6s in the RVM of wild-type mice (top). A fiber was implanted on the RVM over the same coordinates to perform fiber-photometry (bottom). (B) GCaMP6s-positive cells in

the RVM (green) to demonstrate successful expression of GCaMP6s in the $RVM_{post\text{-}LHA}$ neurons. (C) Z-Score of calcium dynamics recorded from the $RVM_{post\text{-}LHA}$ neurons while the mice are restrained and struggling (blue dashes) in a falcon tube. (D) Average plot (individual trials) of Z-Score traces (4 mice, 16 trials) during struggle bouts of $RVM_{post\text{-}LHA}$ neurons. (E) (Left to right) Heatmaps depicting neural activity patterns during individual instances of struggle in the falcon tube, licks, and shakes on the hot plate at 52 degrees, respectively (4 mice, 16 trials). (F) Z-Score of calcium dynamics recorded from the $RVM_{post\text{-}LHA}$ neurons while the mice are on the hotplate set at a gradient from 32-52 degrees. (G) Average plot (individual trials) of Z-Score traces (4 mice, 16 trials) during tail flick assay of $RVM_{post\text{-}LHA}$ neurons.

Figure 8. Activation of $RVM_{post\text{-}LHA}$ neurons resulted in thermal hyperalgesia, while inhibition was anti-nociceptive. (A) AAVTransyn-Cre injected in the LHA and DIO-hM3Dq-mCherry/DIO-tdTomato in the RVM of wild-type mice. (B) DCZ induced c-Fos (green) expression in the $RVM_{post\text{-}LHA\text{-}hM3Dq}$ (red) neurons (zoom-in shown on the right with overlapping cells marked using arrowheads). (C) Tail-flick latency (seconds) (3.22±0.08 compared to 2.69±0.09, respectively; t-test, ***P=0.0001, n=7) post saline or DCZ administration in the $RVM_{post\text{-}LHA\text{-}hM3Dq}$ mice, with no significant difference in $RVM_{post\text{-}LHA\text{-}tdTomato}$ mice. (D) Number of licks (4.57±1.27 compared to 8.43±0.87, respectively; t-test, **P=0.0062, n=7), and latency to lick (seconds) (23.57±7.12 compared to 12.29±2.68, respectively; t-test, *P=0.0466, n=7) post saline or DCZ administration in the $RVM_{post\text{-}LHA\text{-}hM3Dq}$ mice, with no significant difference in $RVM_{post\text{-}LHA\text{-}tdTomato}$ mice. (E) AAVTransyn-Cre injected in the LHA and DIO-hM4Di in the RVM of wild-type mice to express the inhibitory DREADD in the $RVM_{post\text{-}LHA}$ neurons. (F) hM3Dq-mCherry expressing neurons (red) in the RVM. (G) Tail-flick latency (seconds) (2.40±0.11 compared to 3.38±0.23, respectively; t-test, **P=0.0025, n=7) post saline or DCZ administration in $RVM_{post\text{-}LHA\text{-}hM4Di}$ mice. (H) Number of licks (12.00±0.62 compared to 6.86±0.67, respectively; t-test, ***P= 0.0001, n=7), and latency to lick (seconds) (12.14±1.42 compared to 18.86±0.86, respectively; t-test, **P=0.0016, n=7) post saline or DCZ administration in $RVM_{post\text{-}LHA\text{-}hM4Di}$ mice. (I) AAVTransyn-Cre injected in the LHA and DIO-hM4Di in the PBN (bilaterally) of wild-type mice to express the inhibitory DREADD, hM4Di in the $LPBN_{post\text{-}LHA}$ neurons. (J) hM4Di-mCherry (red) expressing neurons in the PBN. (K) Tail-flick latency (seconds) post-saline or DCZ administration in the $PBN_{post\text{-}LHA\text{-}hM4Di}$ mice. (L) Number and latency of licks (seconds) post-saline or DCZ administration in the $PBN_{post\text{-}LHA\text{-}hM4Di}$ mice. (M) AAVTransyn-Cre injected in the LHA and DIO-eNPHR3.0-YFP/DIO-GFP in the RVM of wild-type mice to label the $RVM_{post\text{-}LHA}$neurons. Optic fiber cannulae was implanted over the RVM at same coordinates to deliver yellow light. The summary of the fiber placements are graphically represented (right corner). (N) YFP-positive cells expressing eNpHR3.0 in the $RVM_{post\text{-}LHA}$ (green) neurons in the RVM. (O) Tail-flick latency (seconds) (2.48±0.04 compared to 3.00±0.03, respectively; t-test, ***P=0.0001, n=7) with (ON) and without (OFF) yellow light illumination in $RVM_{post\text{-}LHA}$eNPHR3.0-YFP mice, with no significant difference seen in $RVM_{post\text{-}LHA}$DIO-GFP mice. (P) Number of licks (11.14±1.01 compared to 5.00±0.49, respectively; t-test, ***P=0.0001, n=7), and latency to lick (seconds) (12.71±0.52 compared to 22.86±1.18, respectively; t-test, ***P=0.0001, n=7) with (ON) and without (OFF) yellow

light illumination in $RVM_{post\text{-}LHA}$eNPHR3.0-YFP mice, with no significant difference seen in $RVM_{post\text{-}LHA}$DIO-GFP mice.

Supplementary Fig. 1. (A) Blood corticosterone levels in mice administered with saline, DCZ, or subjected to RS. (B) Sample traces demonstrating time spent by dLSGad67-hM3Dq mice in the lit chamber of the classic light-dark box assay to test stress-induced anxiety. (C) Time spent in the light box post-saline or DCZ administration (35.83±2.59 compared to 26.17±1.35, respectively; t-test, ***P*=0.00578, n=6). (D) Sample traces demonstrating activity of dLSGad67-hM3Dq mice in an open field test. (E) Percentage of time spent by dLSGad67-hM3Dq mice in the centre of the open field (55.33±3.21 compared to 23.17±2.36, respectively; t-test, ****P*=0.0001, n=6). (F) Percentage response of mice to the von Frey Filament Test (63.89±11.72 compared to 19.44±10.01, respectively; t-test, **P*=0.0365, n=5). (G and H) Number and latency (seconds) of jumps post saline or DCZ administration on the hot plate in dLSGad67-tdTomato and dLSGad67-hM3Dq mice. (I) Gad67-Cre and DIO-ChR2-YFP/DIO-GFP injected in the dLS of wild-type mice to label the dLSvgatneurons with the opsin. Optic fiber cannulae was implanted over the dLS at the same coordinates to deliver blue light. (J) YFP-positive cells (green) observed in the dLSvgat neurons (zoom-in shown in the box). (K) Tail-flick latency (seconds) (2.27±0.05 compared to 3.03±0.03, respectively; t-test, ****P*=0.0001, n=5) with (ON) and without (OFF) blue light illumination in dLSGad67-ChR2 neurons, with no significant difference in dLSGad67-GFP mice. (L) Number (10.43±1.00 compared to 2.86±0.51, respectively; t-test, ****P*=0.0001, n=5) and latency of licks (seconds) (10.57±0.57 compared to 20.14±0.74, respectively; t-test, ****P*=0.0001, n=5) with (ON) and without (OFF) yellow light illumination in dLSGad67-ChR2 neurons, with no significant difference in dLSGad67-GFP mice.

Supplementary Fig. 2. (A) Tail-flick latencies (seconds) over an hour of dLSGad67-ChR2 mice post blue light illumination for 30 minutes (2.33±0.05 compared to 2.74±0.01, respectively; Immediate t-test, **P*=0.0321, n=4) (2.34±0.06 compared to 2.85±0.02, respectively; Post-10 minutes t-test, ***P*=0.00877, n=4) (2.37±0.06 compared to 2.98±0.06, respectively; Post 30 minutes t-test, ***P*=0.00832, n=4). (B) Tail-flick latencies (seconds) of mice with and without restraint at different time points post the RS assay (2.27±0.04 compared to 2.73±0.03, respectively; Immediate t-test, **P*=0.0437, n=4) (2.30±0.05 compared to 2.87±0.06, respectively; Post-10 minutes t-test, ***P*=0.0057, n=4) (2.29±0.05 compared to 2.97±0.03, respectively; Post 30 minutes t-test, ***P*=0.0061, n=4). (C) AAVs encoding Gad67-Cre, DIO-hM3Dq-mCherry, and DIO-TetTox-GFP or DIO-GFP injected in the dLS of wild-type mice to simultaneously label the dLSGad67 neurons with the excitatory DREADD, and TetTox. Overlapping yellow cells representing hM3Dq (red), and TetTox (green) co-expressing neurons in the dLS. (D) Tail-flick latency (in seconds) in dLSGad67-TetToxGFP-hM3Dq mice (2.45±0.07 compared to 2.99±0.05, respectively; t-test, ***P*=0.00943, n=4), and in dLSGad67-TetTox-hM3Dq mice post saline or DCZ administration. (E) Gad67-cre and DIO-Tettox-GFP/DIO-GFP injected in the dLS of wild-type mice. (F and G) Number and latency (in seconds) of jumps with and without restraint.

Supplementary Fig. 3. (A and B) Average plot and heat map of dLS GCaMP transients for home cage activity. (C and D) Average plot and heatmap (individual trials) of Z-Score traces (5 mice, 16 trails) during immobilization. (E and F) Average plot and heatmap (individual trials) of Z-Score traces (5 mice, 18 trials) during tail suspension.

Supplementary Fig. 4. (A) AAVs encoding Gad67-Cre and DIO-SynRuby injected in the dLS of wild-type mice. (B) Ruby expression was seen at the injection site and post-synaptic region (LHA), marked region on LHA shown in zoom-in on the right with synapses marked with arrowheads. (C) Rostral to caudal serial images of the LHA taken on a fluorescence microscope at 4X and 10X magnifications showing projections from the dLS, post Gad67-Cre and DIO-GFP injections in the dLS of wild-type mice.

Supplementary Fig. 5. (A) Absorption spectra for the vehicle Dimethysulfoxide (DMSO) (green) and CNO dissolved in DMSO (red). (B) Cy3 fluorescent beads as seen under the microscope at 100X with oil immersion. (C) Cy3 fluorescent beads injected in the dLS and images under the fluorescence microscope at 4X and 10X magnifications (marked region on dLS shown in zoom-in on the bottom). (D) Gad67-Cre and DIO-hM3Dq-mCherry stereotaxically injected in the dLS of wild-type mice to express the excitatory DREADD. 3 weeks later, CNO beads were injected stereotaxically in the dLS over the same coordinates. cFos expression was muted before MP-CNO delivery, increased after 4 days, while reduced on the 8th day of delivery (4.40±1.69 compared to 61.65±3.99, respectively; Control vs Day 4 One-way ANOVA test, ***P=0.0001, n=5), 61.65±3.99 compared to 8.69±5.31, respectively; Day 4 vs Day 8 One-way ANOVA test, **P=0.0048, n=5). (E) Tail-flick latency (seconds) (2.28±0.16 compared to 2.95±0.16, respectively; Day2 One-way ANOVA test, **P= 0.00765, n=7) (2.28±0.16 compared to 3.10±0.22, respectively; Day4 One-way ANOVA test, ***P=0.0001, n=7) over a course of 8 days post CNO beads injection. (F) Number of licks (10.43±1.09 compared to 4.14±1.14, respectively; Day2 One-way ANOVA test, **P=0.00821, n=7) (10.43±1.09 compared to 4.57±1.04, respectively; Day4 One-way ANOVA test, **P=0.0056, n=7), and latency to lick (seconds) (15.14±1.77 compared to 22.57±1.97, respectively; Day2 One-way ANOVA test, *P=0.0328, n=7) (15.14±1.77 compared to 22.57±1.76, respectively; Day4 One-way ANOVA test, *P=0.0412, n=7) over a course of 8 days post CNO beads injection. (G) Gad67-Cre and DIO-tdTomato injected in the dLS of wild-type mice. 3 weeks later, CNO beads were injected stereotaxically in the dLS over the same coordinates. (H) Tail-flick latency (seconds) over the course of 8 days post-CNO beads injection in dLSGad67-hM3Dq mice. (I) Number and latency of licks (seconds) post-CNO beads injection in dLSGad67-hM3Dq mice. (J) Gad67-Cre and DIO-hM3Dq injected in the dLS of wild-type mice. 3 weeks later, CNO beads were injected in the LHA to enable terminal activation of $LHA_{post\text{-}dLS}$ neurons. (K) Tail-flick latency (seconds) (2.49±0.01 compared to 3.05±0.02, respectively; Day2 One-way ANOVA test, ***P=0.0001, n=7) (2.49±0.01 compared to 2.97±0.08, respectively; Day4 One-way ANOVA test, ***P=0.0001, n=7) over a course of 8 days post CNO beads injection. (L) Number of licks (10.83±2.33 compared to 2.17±0.79, respectively; Day2 One-way ANOVA test, *P=0.0435, n=7) (10.83±2.33 compared to 2.17±1.22, respectively; Day4 One-way ANOVA test, *P =0.0387,

n=7), and latency to lick (seconds) (10.50±1.69 compared to 31.33±4.98, respectively; Day2 One-way ANOVA test, *P=0.0245, n=7) (10.50±1.69 compared to 40.50±7.36, respectively; Day4 One-way ANOVA test, **P=0.00456, n=7) over a course of 8 days post CNO beads injection.

Supplementary Figure 6: (A) Allen Brain Atlas images showing the anatomical location of the LHA next to the parasubthalamic nucleus (PSTN) and vglut/vgat expressing cells in the LHA. (B) In situ hybridization using probes against VGlut2 and VGat performed on LHA sections of wild-type mice (red: vglut2, green: vgat) (zoom-in of overlapping cells shown on right with overlap marked using arrowheads). (C) Parvalbumin staining in the LHA sections.

Supplementary Fig. 7. (A and B) Average plot and heatmap (individual trials) of Z-Score traces (5 mice, 12 trials) during immobilization of $LHA_{post\text{-}dLS}$ neurons. (C and D) Average plot and heatmap (individual trials) of Z-Score traces (5 mice, 12 trials) during tail suspension of $LHA_{post\text{-}dLS}$ neurons. (E and F) Average plots and heatmaps for dLS responses on the hot-plate at 32 deg of $LHA_{post\text{-}dLS}$ neurons (5 mice, 12 trials; dotted line indicating time point when mice were placed on the hotplate). (G and H) Average plots and heatmaps for dLS responses on the hot-plate at 52 deg of $LHA_{post\text{-}dLS}$ neurons (5 mice, 12 trials; dotted line indicating time point when mice were placed on the hotplate).

Supplementary Fig. 8. (A) Number and latency to lick before and after RS in wild-type mice i.p. injected with the mu-opioid receptor antagonist naltrexone. (B) Gad67-Cre and DIO-hM3Dq injected in the dLS of wild-type mice to express the excitatory DREADD, hM3Dq in the dLSGad67 neurons. (C) Number and latency (in seconds) of licks post-saline or DCZ administration in dLSGad67-hM3Dq mice post i.p. Naltrexone administration. (D) AAVTransyn-Cre injected in the LHA, and DIO-SynRuby injected in the RVM of wild-type mice. (E) Red cell bodies expressing SynRuby were observed in the RVM (zoom-in of maeked region shown on the right). (F) Red puncta of $RVM_{post\text{-}LHA}$ axon terminals observed in the LHA (zoom-in of marked region shown on the right). (G) Axon terminals of the $RVM_{post\text{-}LHA}$ neurons seen in the dorsal horn of the lumbar spinal cord (* marking distinct neurons).

Supplementary Fig. 9. (A) DIO-SynGFP injected in the LHA, and DIO-PSD95-tagRFP in the RVM of VGlut2-Cre transgenic mice. (B) Confocal images of the LHA^{VGlut2} terminals (green), and RVM^{VGlut2} dendrites (red) observed under 10X magnification. (C) Confocal images under 20X magnification of the same regions (closely apposed green and red cells marked with arrowheads, zoom-in on the right). (D) 40X Airyscan superresolution image demonstrating close apposition between the red, and green puncta (closely apposed green and red cells marked with arrowheads, zoom-in on the right). (E) Bar graph depicting the AUC of the photometry recordings during the struggle bouts from dLS^{Gad67}, $LHA_{post\text{-}dLS}$, and $RVM_{post\text{-}LHA}$ neurons. (F) Diagrammatic representation of the dLS-centric RS-induced SIA pathway that originates from dLS and terminates in the spinal cord via LHA and RVM.

Figure 1

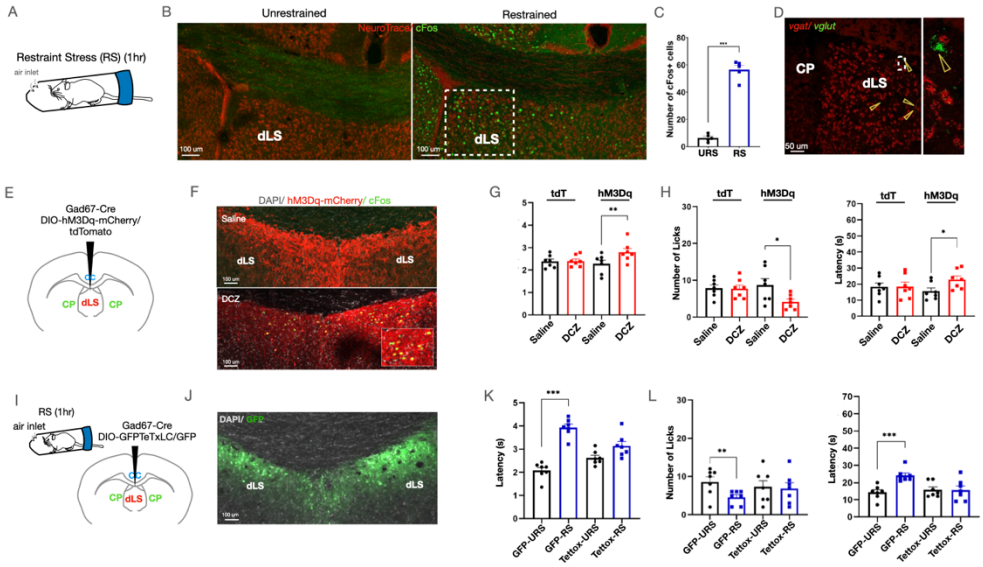
A
Restraint Stress (RS) (1hr)
air inlet
B
Unrestrained
Restrained
NeuroTrace
cFos
dLS
100 um
C
Number of cFos+ cells
URS
RS
D
vgat/ vglut
CP
dLS
50 um
E
Gad67-Cre
DIO-hM3Dq-mCherry/
tdTomato
CP
dLS
F
DAPI/ hM3Dq-mCherry/ cFos
Saline
DCZ
G
tdT
hM3Dq
Saline
DCZ
H
Number of Licks
Latency (s)
I
RS (1hr)
Gad67-Cre
DIO-GFPTeTxLC/GFP
J
DAPI/ GFP
K
GFP-URS
GFP-RS
Tetox-URS
Tetox-RS
L

Figure 2

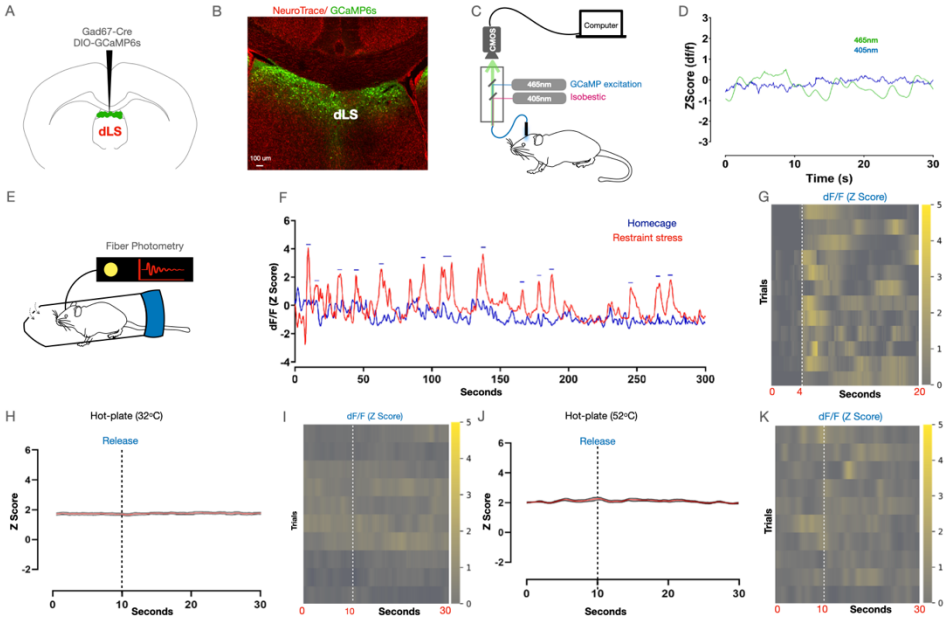
A
Gad67-Cre
DIO-GCaMP6s
dLS
B
NeuroTrace/ GCaMP6s
dLS
100 um
C
Computer
CMOS
465nm
405nm
GCaMP excitation
Isobestic
D
465nm
405nm
ZScore (df/f)
Time (s)
E
Fiber Photometry
F
Homecage
Restraint stress
dF/F (Z Score)
Seconds
G
dF/F (Z Score)
Trials
Seconds
H
Hot-plate (32°C)
Release
Z Score
Seconds
I
dF/F (Z Score)
Trials
Seconds
J
Hot-plate (52°C)
Release
Z Score
Seconds
K
dF/F (Z Score)
Trials
Seconds

Figure 3

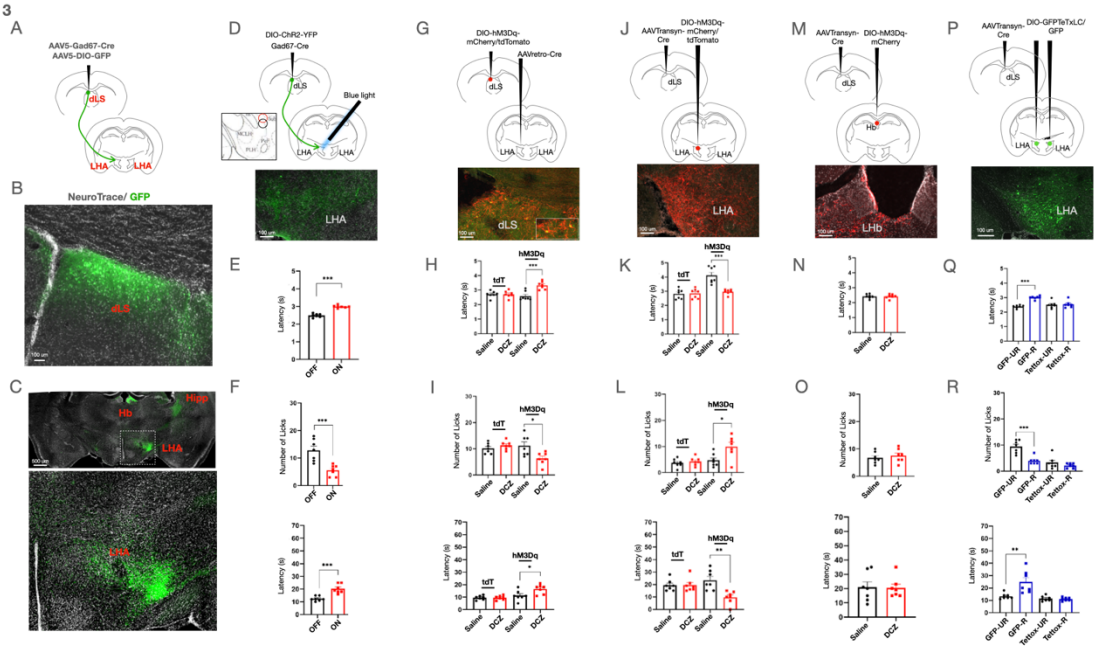
A
AAV5-Gad67-Cre
AAV5-DIO-GFP
dLS
LHA
LHA
B
NeuroTrace/ GFP
dLS
C
Hb
Hipp
LHA
LHA
D
DIO-ChR2-YFP
Gad67-Cre
dLS
Blue light
LHA
LHA
LHA
E
Latency (s)
OFF
ON
F
Number of Licks
Latency (s)
G
DIO-hM3Dq-mCherry/tdTomato
AAVretro-Cre
dLS
LHA
LHA
dLS
H
hM3Dq
tdT
Latency (s)
Saline
DCZ
Saline
DCZ
I
Number of Licks
Latency (s)
J
AAVTransyn-Cre
DIO-hM3Dq-mCherry/tdTomato
dLS
LHA
LHA
LHA
K
Latency (s)
L
Number of Licks
Latency (s)
M
AAVTransyn-Cre
DIO-hM3Dq-mCherry
dLS
Hb
LHb
N
Latency (s)
O
Number of Licks
Latency (s)
P
AAVTransyn-Cre
DIO-GFPTeTxLC/GFP
dLS
LHA
LHA
LHA
Q
Latency (s)
GFP-UR
GFP-R
Tetox-UR
Tetox-R
R
Number of Licks
Latency (s)

Figure 4

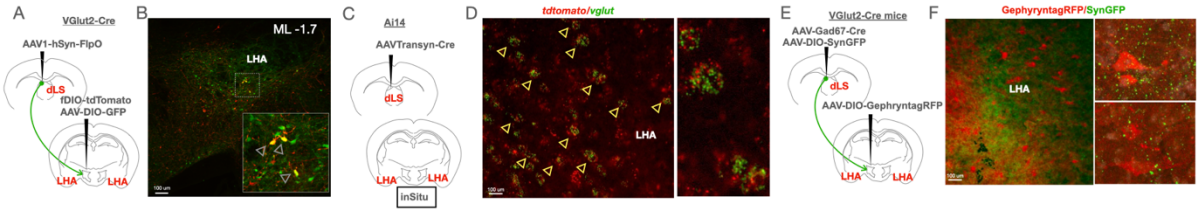
A
VGlut2-Cre
AAV1-hSyn-FlpO
dLS
fDIO-tdTomato
AAV-DIO-GFP
LHA
LHA
B
ML -1.7
LHA
C
Ai14
AAVTransyn-Cre
dLS
LHA
LHA
inSitu
D
tdtomato/vglut
LHA
E
VGlut2-Cre mice
AAV-Gad67-Cre
AAV-DIO-SynGFP
dLS
AAV-DIO-GephryntagRFP
LHA
LHA
F
GephyryntagRFP/SynGFP
LHA

Figure 5

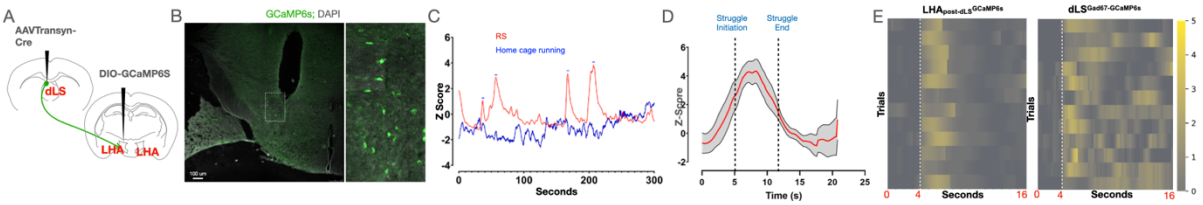
A
AAVTransyn-Cre
DIO-GCaMP6S
dLS
LHA
LHA
B
GCaMP6s; DAPI
C
RS
Home cage running
Z Score
Seconds
D
Struggle Initiation
Struggle End
Z-Score
Time (s)
E
LHApost-dLSGCaMP6s
dLSGad67-GCaMP6s
Trials
Seconds

Figure 6

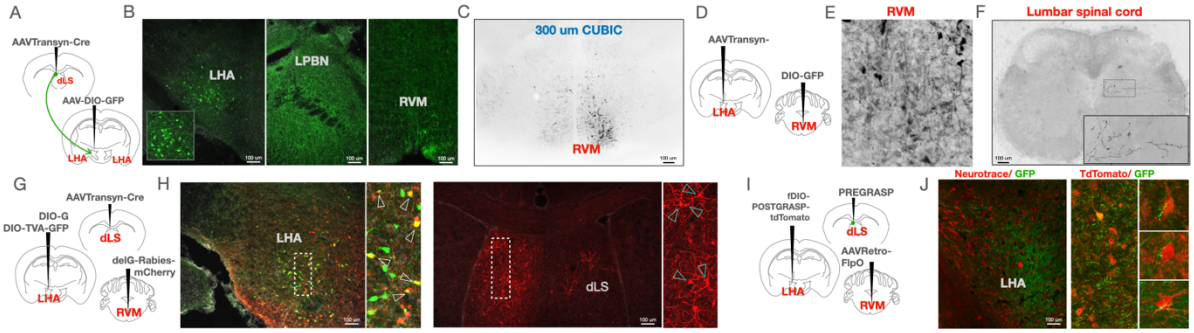
A
AAVTransyn-Cre
dLS
AAV-DIO-GFP
LHA
LHA
B
LHA
LPBN
RVM
C
300 um CUBIC
RVM
D
AAVTransyn-
DIO-GFP
LHA
RVM
E
RVM
F
Lumbar spinal cord
G
AAVTransyn-Cre
DIO-G
DIO-TVA-GFP
dLS
delG-Rabies-
mCherry
LHA
RVM
H
LHA
dLS
I
fDIO-
POSTGRASP-
tdTomato
PREGRASP
dLS
AAVRetro-
FlpO
LHA
RVM
J
Neurotrace/ GFP
TdTomato/ GFP
LHA

Figure 7

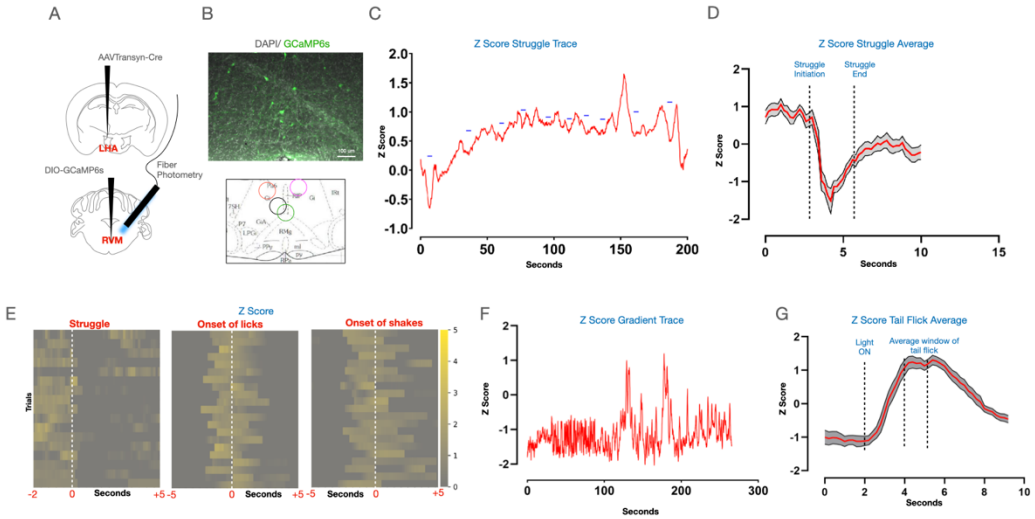
A
AAVTransyn-Cre
LHA
DIO-GCaMP6s
Fiber Photometry
RVM
B
DAPI/ GCaMP6s
C
Z Score Struggle Trace
Z Score
Seconds
D
Z Score Struggle Average
Struggle Initiation
Struggle End
Z Score
Seconds
E
Z Score
Struggle
Onset of licks
Onset of shakes
Trials
Seconds
F
Z Score Gradient Trace
Z Score
Seconds
G
Z Score Tail Flick Average
Light ON
Average window of tail flick
Z Score
Seconds

Figure 8

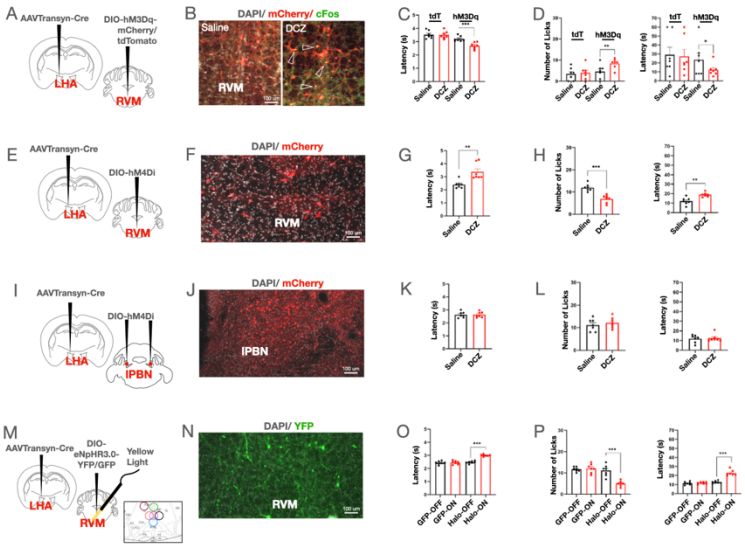
A
AAVTransyn-Cre
DIO-hM3Dq-mCherry/tdTomato
LHA
RVM
B
DAPI/ mCherry/ cFos
Saline
DCZ
RVM
C
tdT
hM3Dq
Latency (s)
Saline
DCZ
D
Number of Licks
Latency (s)
E
AAVTransyn-Cre
DIO-hM4Di
LHA
RVM
F
DAPI/ mCherry
RVM
G
Latency (s)
H
Number of Licks
Latency (s)
I
AAVTransyn-Cre
DIO-hM4Di
LHA
IPBN
J
DAPI/ mCherry
IPBN
K
Latency (s)
L
Number of Licks
Latency (s)
M
AAVTransyn-Cre
DIO-eNpHR3.0-YFP/GFP
Yellow Light
LHA
RVM
N
DAPI/ YFP
RVM
O
Latency (s)
GFP-OFF
GFP-ON
Halo-OFF
Halo-ON
P
Number of Licks
Latency (s)

Supplementary Figure 1

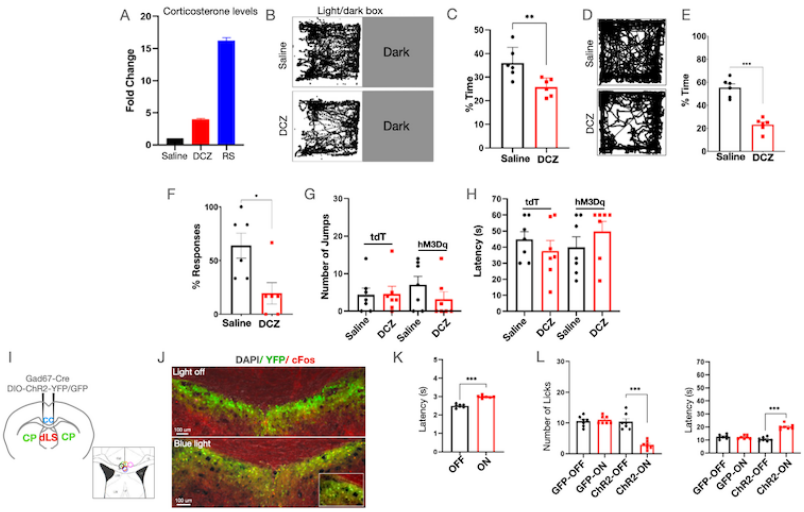

Supplementary Figure 2

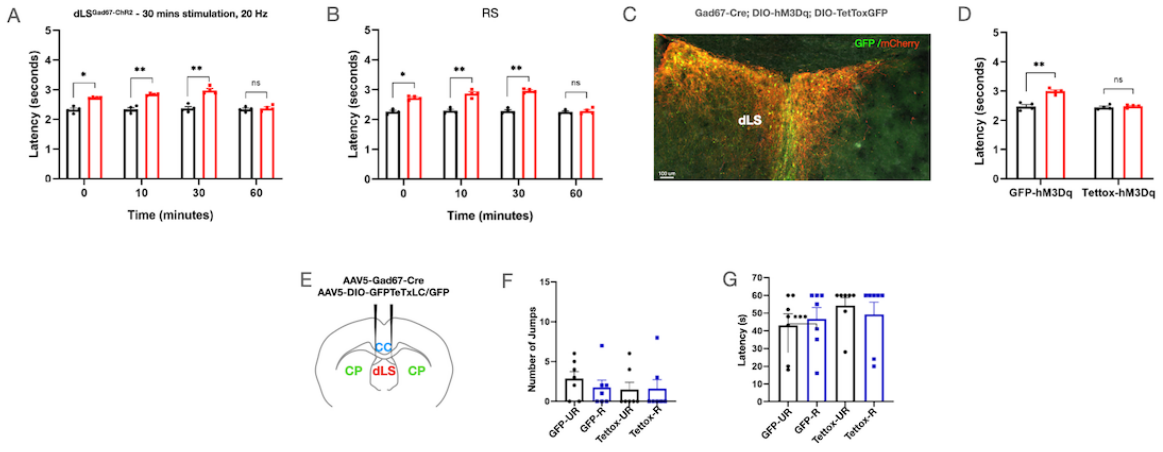

Supplementary Figure 3

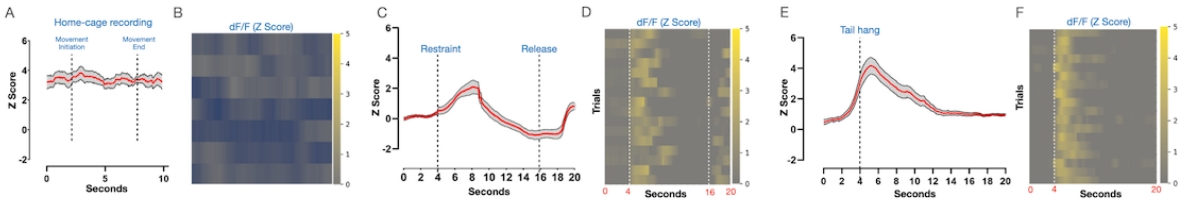

Supplementary Figure 4

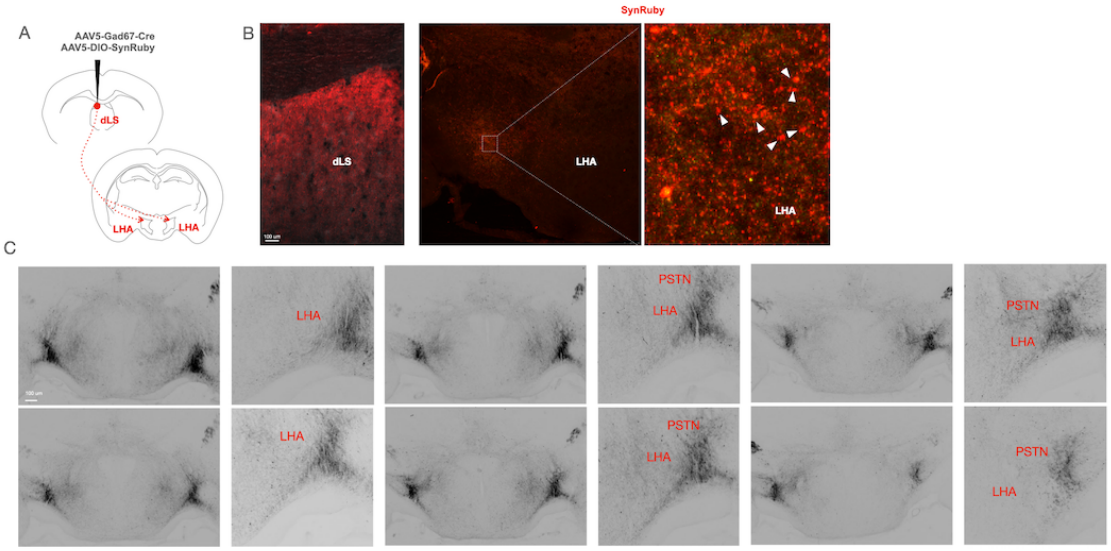

Supplementary Figure 5

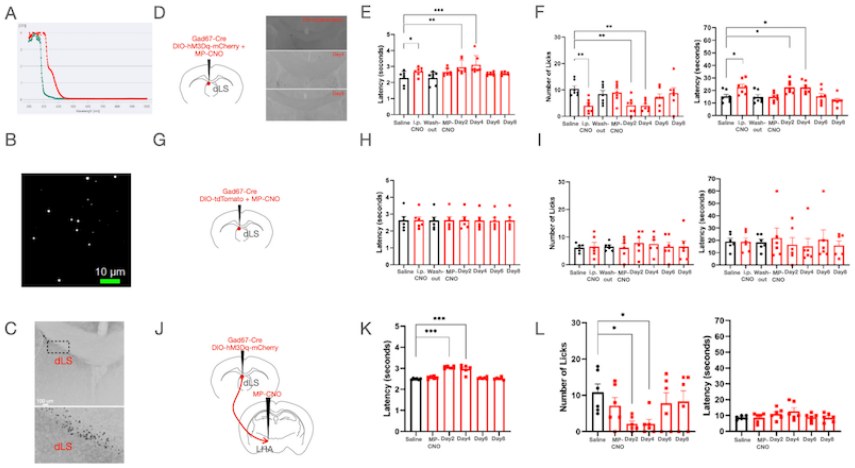

Supplementary Figure 6

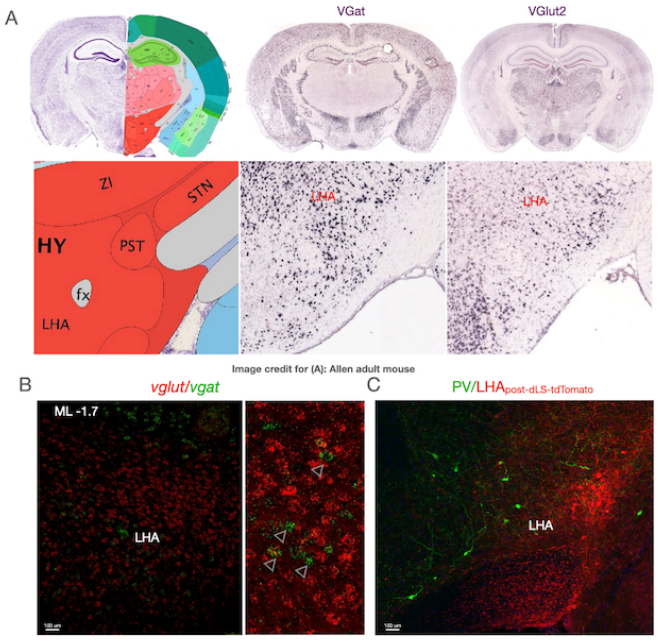

Supplementary Figure 7

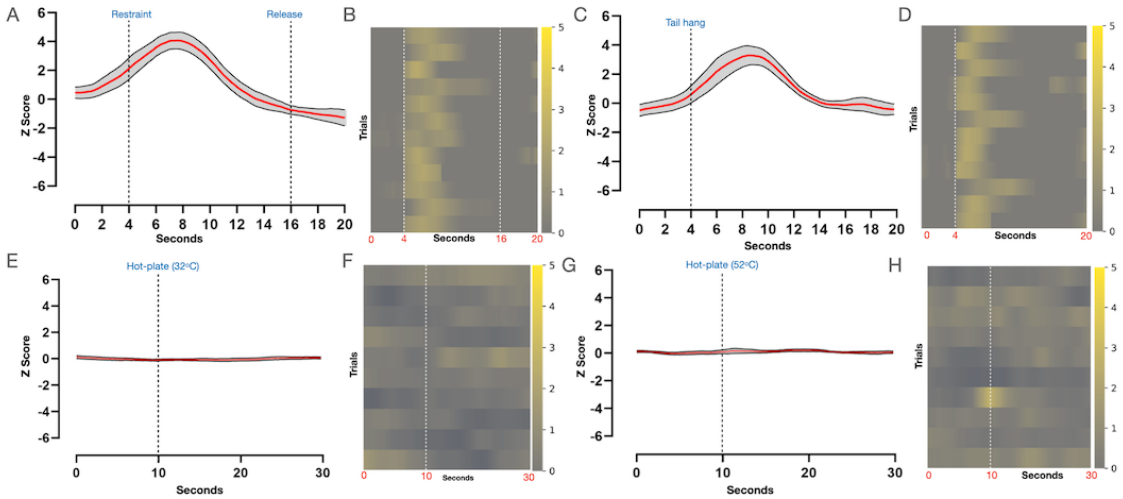

Supplementary Figure 8

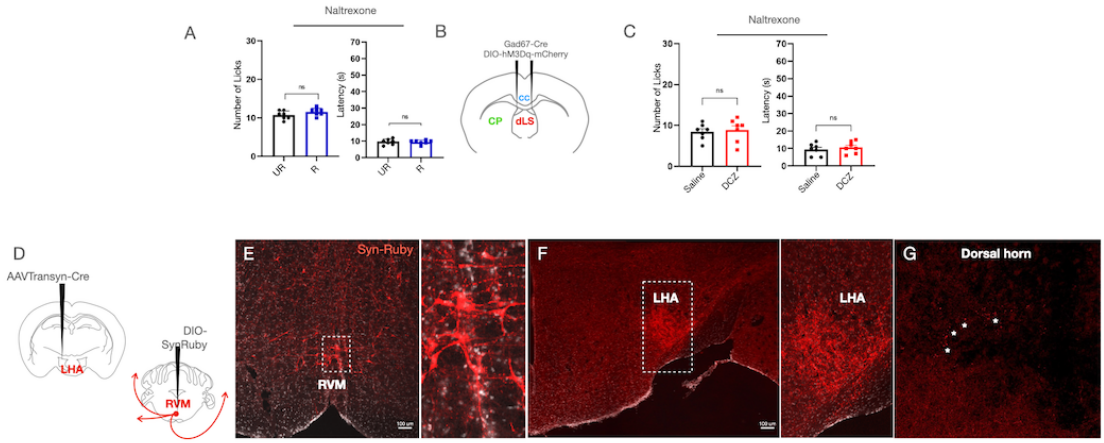

Supplementary Figure 9

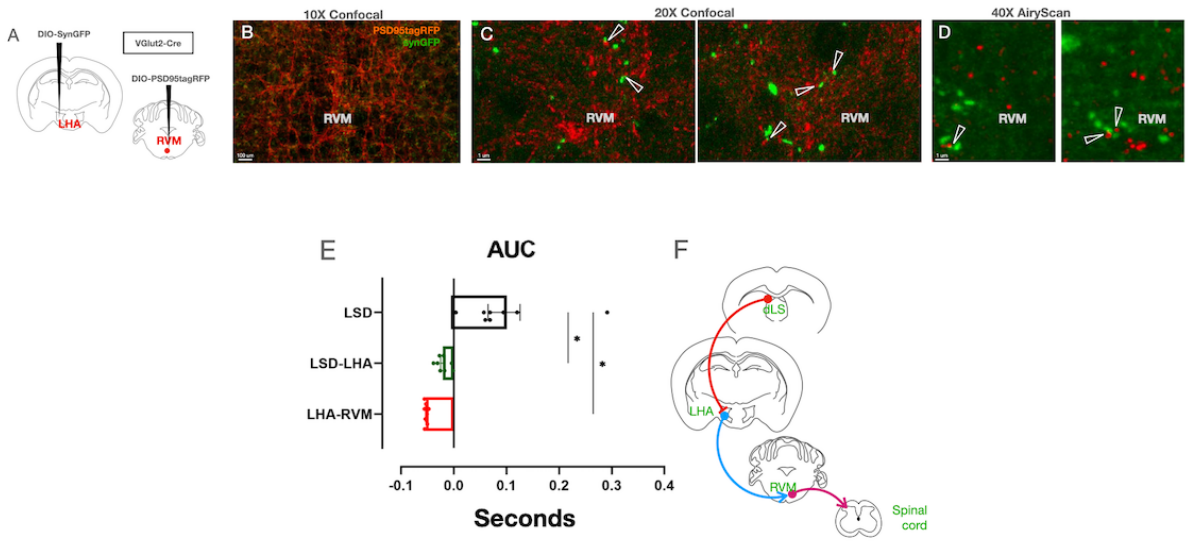

List of Abbreviations:

BSA – Bovine Serum Albumin
CFA – Complete Freund's adjuvant
ChR2 – Channel rhodopsin 2
CNO – Clozapine N-Oxide
DCM – Dichloromethane
DCZ – Deschloroclozapine
dLS – dorsal Lateral Septum
DMSO – Dimetlysulfoxide
DREADD – Designer Receptors Exclusively Activated by Designer Drugs
DRN – Dorsal Raphe nucleus
ELISA – Enzyme-linked immunosorbent assay
GABA – Gamma-aminobutyric acid
GAD67 - Glutamic acid decarboxylase
GFP – Green Fluorescence protein
GPU – Graphics Processing Unit
Hipp – Hippocampus
HRP – Horseradish peroxidase
i.p. – Intraperitoneal
ISH – In-situ hybridization
LHA – Lateral Hypothalamic Area
LHb – Lateral Habenula
LPBN – Lateral parabrachial nucleus
MP – Microparticle
O.D. – Optical Density
PAG – Periaqueductal gray
PBS – Phosphate Buffered Saline
PFA – Paraformaldehyde
PLGA – Poly-DL-lactic-co-glycolic
PV – Parvalbumin
PVA – polyvinyl alcohol
RS – Restraint Stress
RVM – Rostral Ventromedial Medulla
SIA – Stress Induced Analgesia
SPF – Specific pathogen-free
TetTox – Tetanus Toxin
TMB – Tetramethylbenzidine
VGat – Vesicular GABA Transporter
Vglut2 – Vesicular glutamate transporter
YFP – Yellow Fluorescence protein